PERFORMANCE ASSESSMENT OF PROTON EXCHANGE MEMBRANE FUEL CELL(PEMFC) STACK BY MEANS OF SEMI-EMPIRICAL MODEL

A Thesis Submitted to
the Graduate School of Engineering and Sciences of
İzmir Institute of Technology
in Partial Fulfillment of the Requirements for the Degree of

MASTER OF SCIENCE

in Energy Engineering

by
Eda KALENDER

June 2011
İZMİR

We approve the thesis of **Eda KALENDER**

_____

Prof.Dr.Barış ÖZERDEM
Supervisor

_____

Prof.Dr.Zafer İLKEN
Committee Member

_____

Assist.Prof.Dr.Zehra ÖZÇELİK
Committee Member

29 June 2011

_____

Assoc.Prof.Dr.Gülden GÖKÇEN AKKURT
Head of the Department of Energy Engineering

_____

Prof.Dr.Durmuş Ali DEMİR
Dean of the Graduate School of Engineering and Sciences

ACKNOWLEDGMENTS

I would like to thank primarily to my supervisor Prof. Dr. Barış Özerdem for his continual support and valuable advices throughout my thesis completion. I am really grateful to my co-advisor Georgios Tsotridis who is Fuel Cell Action Leader at Institute for Energy (IE), Joint Research Center, Netherlands to provide me the opportunity of working with his well-qualified Fuel Cell Action team.

I would like to also appreciate to Thomas Malkow, Michel Honselaar, Giancarlo de Marco, Antonio Saturnio, Alberto Pilenga, Krissimir Koutzarov and Ivan Radev for their valuable knowledge about fuel cells and assist me on my thesis.

During my thesis study at Netherlands, I am really thankful to my friends Betül Gülçimen and Nermana Bulic to keep alive unforgettable and enjoyable shares from time to time taking my mind off my thesis. I would like to express many thanks to my sincere friends, Merve Şamlı, Manolya Akdemir, Aslı Küçük, Özgür Çekmer, Taner Erdoğan, Okan Depboylu and Emre Kılıç. My last and the most valuable thanks are to my family for their eternal support and trust to me.

ABSTRACT

PERFORMANCE ASSESSMENT OF PROTON EXCHANGE MEMBRANE FUEL CELL(PEMFC) STACK BY MEANS OF SEMI-EMPIRICAL MODEL

In this study, the performance of a 10 kW peak power proton exchange membrane fuel cell stack under different operating conditions was investigated experimentally by its i-V polarization curve. The stack has been fed with pure hydrogen and air and PEM fuel cell stack has active area 200 cm^2 and is composed of 75 single cells. The stack was tested for different reactant inlet temperatures as from 50 °C to 65 °C with 5 °C intervals keeping constant other conditions and for different relative humidities as 75%, 85% and 95% again keeping constant other operation conditions. Then the analytical nonlinear model adapted to describe the polarization curve has been discussed. Model parameters have been simultaneously estimated by fitting data into model by using LABFIT nonlinear regression program. These parameters are the cathode exchange current density, charge transfer coefficient and polymer electrolyte membrane internal resistance.

The polarization curve of the fuel cell stack showed the stack performance improved from 50 °C to 65 °C temperature with the decrease of voltage losses. However the decrease of relative humidity from 95% to 75% did not show any explicit effect onto stack performance. Data fitting was obtained with reasonable model parameters in accordance with literature and with high coefficient of determination (R^2) values. The effect of temperature on model parameters was also investigated. The cathode exchange current density value increased from 2.247×10^{-6} A/cm^2 at T=50 °C to 5.643×10^{-6} A/cm^2 at T=65 °C. The charge transfer coefficient estimated around 0.4 coherently with literature. The membrane internal resistance value followed the slightly decreasing tendency with increasing temperature as the value around 0.1 Ω cm^2.

ÖZET

YARI DENEYSEL MODEL İLE PROTON DEĞİŞİM MEMBRAN YAKIT PİLİ(PDMYP) YIĞININ PERFORMANS DEĞERLENDİRİLMESİ

Bu çalışmada 10 kW maksimum güç değerindeki proton değişim membran yakıt pili yığınının değişen çalışma koşulları altında deneysel olarak i-V polarizasyon eğrisi ile performansı incelenmiştir. Yığın, saf hidrojen ve hava ile beslenmektedir. Proton değişim membran yakıt pili yığını 200 cm^2 aktif alana sahip olup, 75 yakıt pili hücresinden oluşmaktadır. Yakıt pili yığını, diğer koşullar sabit tutularak 5 °C aralıklarla 50 °C 'den 65 °C 'ye kadar farklı reaktan giriş sıcaklıkları ve 75%, 85% ve 95% bağıl nemlilik için yine diğer çalışma koşullarının sabit tutulmasıyla test edilmiştir. Deneysel verilerin değerlendirilmesinden sonra, polarizasyon eğrisini tanımlayan doğrusal olmayan analitik model incelenmiştir. Model parametreleri, LABFIT doğrusal olmayan regresyon programıyla eşanlı olarak deneysel verinin modele uydurulmasıyla ile aynı anda tahmin edilmiştir. Bu parametreler; katot değişim akım yoğunluğu, yük değişim katsayısı ve polimer elektrolit membran iç direncidir.

Yakıt pili yığınından elde edilen polarizasyon eğrisine göre, sıcaklık 50 °C 'den 65 °C 'e yükseldiğinde voltaj kayıplarının azalmasıyla yığın performansının arttığı görülmektedir. Ancak bağıl nemliliğin 95% 'den 75% 'e azalması yığının performansında önemli bir değişim yaratmamıştır. Verinin modele uydurulması sonucu literatüre uygun model parametreleri ve yüksek belirleme katsayısı (R^2) değerleri elde edilmiştir. Sıcaklığın model parametrelerine etkisi de bu çalışmada incelenmiştir. Katot değişim akım yoğunluğu, 50 °C sıcaklıkta 2.247×10^{-6} A/cm^2 değerinden, 65 °C' de 5.643×10^{-6} A/cm^2'ye artmıştır. Değişim transfer katsayısı 0.4 civarında olarak literatüre uygun olarak tahmin edilmiştir. Membran iç direnci ise 0.1 Ω cm^2 civarında olup, artan sıcaklıkla hafif azalan bir eğilim izlemiştir.

TABLE OF CONTENTS

LIST OF FIGURES

Figure **Page**

LIST OF TABLES

LIST OF SYMBOLS

A	active surface cell area, cm^2
C_B	bulk concentration of reactant, mol/cm^3
C_S	concentration of the reactant at the catalyst surface, mol/cm^3
D	diffusion coefficient or diffusivity, cm^2/s
E	voltage based on the concept of electromotive force, V
E^0	reversible open circuit voltage at standard pressure, V
$E_o^{\ 0}$	standard state reference potential, V
E_{rev}	thermodynamically calculated reversible voltage, V
F	Faraday constant, $96487\ C/mol$
G	Gibbs free energy, J/mol
HHV	higher heating value for H_2, kJ/mol
i	current density, mA/cm^2
i_o	exchange current density, mA/cm^2
$i_{o,c}$	cathode exchange current density, mA/cm^2
i_L	limiting current density, mA/cm^2
I	current, A
J	diffusion flux per unit time, mol/s
k	number of the experimental data points
L	thickness of membrane, cm
LHV	lower heating value for H_2 , kJ/mol
M	molar mass of dry reactant gas, g/mol
N	number of cells in the stack
m and n	parameters relating to mass diffusion loss
$P_{H_2}^{\bullet}$	partial pressure of hydrogen at the catalytic interface of the anode, atm
$p_{H_2O}^{sat}$	saturation pressure of water vapor, bar
$P_{O_2}^{\bullet}$	partial pressure of oxygen at the catalytic interface of the cathode, atm
$Q_{v,\lambda}$	volumetric flow rate (dry basis) of the reactant, l/min
R	universal gas constant , 8.314 $J/(mol\ K)$
$R_{electronic}$	resistance to electron flow in the electrodes, $\Omega\ cm^2$
$R_{\ int}$	area-specific resistance to ion flow inside the electrolyte, $\Omega\ cm^2$
r_M	membrane-specific resistivity for the flow of hydrated protons, $\Omega\ cm$

S^0	standard state entropy, *J /K*
T	fuel cell operation temperature, *K*
$V_{act,a,}$ $V_{act,c}$	activation loss on the anode and cathode electrode respectively, *Volt*
V_{ohmic}	ohmic loss, *Volt*
$V_{con,a}$, $V_{con,c}$	concentration loss on the anode and cathode respectively, *Volt*
W_e	electrical work , *J/mol*
x	the distance that the object is diffusing, cm
$X_{H_2O}^{anode}$	molar fraction of water at saturation at anode electrode side
$X_{H_2O}^{cathode}$	molar fraction of water at saturation at cathode electrode side
z	the electron transfer number in the electrochemical reaction

Greek Letters

α	charge transfer coefficient
γ	stoichiometric ratio
δ	ratio of excess to required amount of inlet reactants (fuel and air)
ε	parametric coefficients based on the experimental data involved in activation and ohmic loss
λ	adjustable fitting parameter relating to ionic resistance
ρ	density of dry reactant gas under standard conditions, g/dm^3
φ	hydrogen or oxygen content in the dry gas mixture

CHAPTER 1

INTRODUCTION

Energy has a paramount importance for today's modern industrialized economy. All our welfare depends totally on the sufficient, uninterrupted supply of energy. Worldwide energy demand continues to grow at an alarming rate. The European 'World Energy Technology and Climate Policy Outlook'(WETO) estimates an average primary energy demand growth rate of 1.8% per annum for the period 2000-2030. This increasing demand is largely being met by the limited fossil fuel reserves- oil, natural gas, and coal that emit greenhouse gas and other pollutants. Scarcity of fossil sources will ultimately cause fuel prices to rise around the world (European Commission Special Report, 2003). Moreover, these limited fuels -especially oil and gas reserves- are not equally distributed all over the world. A few countries are self-sufficient but most have to import fuels from producers. This dependency has revealed the concept of 'security of energy supply' as a major challenge. The basic idea of the security of supply is to provide a secure transfer of energy supplies from producer countries to consumer countries. This is however not so easy. There are many different relations affecting it such as the domestic energy market's situation, the political stability in the suppliers and transit countries, the stable and acceptable energy prices (Beden, 2007).

Recent energy crisis has necessitated the European Union (EU) to debate on the development of comprehensive European Energy Policy. The Ukraine-Russia gas dispute has increased Europe's concerns about secure supply of energy. Matters of volatile energy prices, the uncertain state of energy reserves, the disequilibrium between the demand and supply prompted the EU to develop an enhanced common approach against supply disruption and to search for new alternatives to mitigate the external energy dependency (Andoura, 2007).

Environmental concerns, as a second challenge, have regularly been rising in the last decades. The emissions from burning fossil fuels are the biggest contributor of anthropogenic greenhouse gas emissions. Measurements of atmospheric concentration of carbon dioxide (CO_2) by far the most predominant energy related greenhouse gas indicate that concentration were stable at approximately 270 parts per million (ppm)

over the biggest part of the last 1000 years. However from the mid 19th century, it significantly increased to attain roughly 378 ppm in 2004. The result is the greenhouse effect, the earth is warming up which causes climates to change (International Energy Agency Report, 2007). Due to security of supply issues and environmental problems, the European Union has developed own energy policy that purposes *'ensuring the uninterrupted physical availability of energy products on the market at an affordable price for all consumers, whilst respecting environmental concerns and looking towards sustainable development'* (Andoura, 2007). This intends to achieve both energy security and environmental policy objectives as efficiently as possible and calls for immediate actions to increase energy efficiency and to promote greenhouse gas emission-free energy sources such as renewable energy sources, alternative fuels for transportation. Hydrogen as an energy carrier together with fuel cell energy converters may offer a promising solution for building up a clean and an efficient energy system that is based on sustainable primary sources such as solar, wind, geothermal energies. In this sustainable way, a remarkable reduction of greenhouse gas emissions is expected (Bleischwitz and Fuhrmann, 2006). In addition, these technologies can support local energy production solutions which increase, the opportunity to use a wide range of local energy sources.

The objective of this study is to assess the performance characteristics of 10 kW proton exchange membrane (PEM) fuel cell stack by changing the load instantenously and observing the voltage variation inside the stack with some voltage losses. The current density versus voltage curve presents the electrical performance behavior of stack. The experiments were conducted with different operation conditions, changing temperature and relative humidity by performing the limitations of manufacturer recommended stack conditions in order to find which condition achieves better performance. The experimental data then is fitted to a nonlinear semi-empirical model for PEM fuel cell stack developed. The model parameters are analysed to understand how these parameters change according to the operation conditions to provide the better stack conditions. Chapter 2 provides an introduction into hydrogen as a fuel, its production and storage technologies and fuel cell technology. The fuel cell type that is mainly considered is the proton exchange membrane (PEM) type of fuel cell which is earmarked as highly promising as power provider for future power vehicles and is explained on the basis of its voltage versus current density performance characteristic. Voltage losses are clearly expressed to understand the analytical formulation of the

steady state nonlinear PEM fuel cell model. Chapter 3 presents a literature survey on model development of nonlinear models. The issue of data fitting into the model is as well provided. Chapter 4 describes the experimental test set-up, procedure and experimental conditions. Chapter 5 assesses the experimental test results according to different temperature conditions as from 50 °C to 65 °C and relative humidity conditions as from 75% to 95% and the data fitting into the model is provided including the model parameters and coefficient of determination results. The model parameters are compared with literature values and their variations with different temperature and relative humidity conditions are interpreted. The results on data fitting and model parameters are also presented.

It is summarised in Chapter 6 as a conclusion that the test results displayed a good data fitting into semi-empirical model with reasonable model parameters as cathode exchange current density, charge transfer coefficient and area specific resistance inside electrolyte in comparison with literature values and coefficient of determination results. The increase of temperature from 50 to 65 °C affects on cathode exchange current densities more than charge transfer coefficient decreasing the activation losses. Internal resistance inside polymer electrolyte membrane decreases by temperature increase hence it decreases ohmic losses. The decrease of relative humidity from 95% down to 75% does not change the voltage versus current density performance characteristic (polarization) graph explicitly.

CHAPTER 2

HYDROGEN AND FUEL CELL TECHNOLOGY

Hydrogen with fuel cell converters are widely considered as a future energy technology particularly for transportation sector. However much efforts are still needed on reduce the costs of all components and systems included in hydrogen economy, increase and improve -performance, manufacturing and infrastructure and -develope, international agreements on regulations, codes and standards in order to make the transition from the research and development stage to the commercialization stage.

2.1. Hydrogen as a Fuel

Hydrogen is not a primary energy source like coal and gas. Although hydrogen is probably the most abundant element in the universe, pure hydrogen (H_2) used for fuel cells does not exist naturally. It must be extracted from hydrogen-rich sources like natural gas, coal or water by different hydrogen production technologies. One another property of hydrogen is the capability of highest energy content per unit weight of any known element (about three times more than gasoline), however lowest volumetric energy density (about four times less than gasoline) which causes storage problems especially for confined systems.

Regarding to hydrogen production and storage technologies, the major issue is to be cost comparable with conventional fuels and technology systems and research is continuously carried out in order to improve hydrogen fuel vehicles. Moreover durability over the performance lifetime of these systems must be validated and acceptable refueling times must be achieved. Infrastructure is required for hydrogen production, storage and distribution and in the case of transportation, special facilities should be built for vehicle refueling. The use of hydrogen-fuelled transport will depend on the successful improvement of an affordable and widespread refueling infrastructure. Recently only a few expensive hydrogen refueling stations exist worldwide and refueling station costs need to be reduced to make them commercially viable (European Commission Special Report, 2003).

2.1.1. Hydrogen Production Methods

Hydrogen can be produced in many diverse ways, using a wide range of technologies like chemical, biological, electrolytic, photolytic and thermo-chemical process (International Energy Agency Report, 2004). Some of these are mature processes whilst others are in a R&D stage. The first commercial hydrogen production technology, dating from the late 1920s was electrolysis of water producing pure hydrogen. In the 1960s an industrial production of hydrogen shifted towards a fossil based feedstock (Riis et al., 2005).

Research is being performed to improve hydrogen production technologies in an economically and environmentally benign way. Currently the most prevalent and least expensive way is steam reforming of natural gas which transform methane (and other hydrocarbons in natural gas) into hydrogen and carbon monoxide by steam over a nickel catalyst. However CO_2 is generated as by-product in this process. If the water electrolyser is used for hydrogen production and the electrolyser is powered by a renewable energy source, through use of a solar panel or a wind turbine, there would be no emissions of carbon dioxide (Cook, 2001). Other methods are still under research and are defined briefly as; high temperature steam electrolysis uses heat (approximately 1000 °C) to supply the required energy to split water, thermo chemical water splitting uses chemicals and heat in multiple steps to split water into its components, photo electrochemical systems use semi-conducting materials (like photovoltaic) to split water using only sunlight, photo-biological systems use micro-organisms to split water using sunlight, biological systems use microbes to break down a variety of biomass feed stocks into hydrogen, gasification utilizes from heat to break down biomass or coal into a gas from which pure hydrogen can be generated (International Partnership for the Hydrogen Economy Fact Sheet).

2.1.2. Hydrogen Storage Methods

Hydrogen can easily be stored at large scales in vessels or underground caverns however for transportation applications a breakthrough for an on-board hydrogen storage has to be realized to get a driving range comparable with conventional diesel or gasoline vehicles. On-board hydrogen storage in the range of approximately 5-13 kg is

required for hydrogen-powered vehicles to enable a driving range of more than 480 kilometers between refueling stops to compete with today's gasoline vehicles (U.S. Department of Energy Hydrogen Program, 2006). A gram of hydrogen gas occupies about 11 liters of space at atmospheric pressure. Therefore in order to obtain a large amount of hydrogen into a small space, high pressures are required however this causes a storage problem, especially within the size and weight constraints of a vehicle. Today's on-board hydrogen storage methods are compressed hydrogen gas tanks and liquid hydrogen tanks. Future storage technologies such as metal hydrides, chemical hydrides and carbon nanotubes are immature yet and still under research. Compressed gas storage tanks currently have capacities of 350 bar and 700 bar. Compressed tanks are reasonable for stationary applications where there is no restriction on size and weight whereas it is less practical for transportation applications due to high weight and cost of compressed metal tanks. Liquefaction of hydrogen is relatively more difficult than other gases. It cannot be simply compressed in the way that LPG or butane can. It has to be cooled down to about 22 K (Larminie and Dicks, 2003). The energy density of hydrogen can be improved by liquefaction. However, the required energy for the liquefaction and the tank cost to hold under pressure and low temperature media makes the cryogenic storage very expensive and also well insulation has to be implemented to prevent the leakage. Metal hydrides use metallic alloys to adsorb hydrogen under moderate pressure and temperature. Although the percent of absorbed gas to the volume of the metal remains largely low, hydrides are anticipated an intriguing technology because they can safely store and deliver extremely pure hydrogen at a constant pressure. Chemical hydrides are slurries or solutions used as hydrogen carrier or storage medium. e.g. Na-BH_4 solution. Research studies investigate an identification of safe, stable slurries and the design of the reactor for regeneration of the spent slurry. Carbon nanotubes are microscopic tubes of carbon, two nanometers across, that store hydrogen in microscopic pores on the tubes. Carbon nanotubes have a wide range of hydrogen storage capacity from 4% up to 65% of their own weight. However being a not fully developed technology it needs to be improved with low-cost manufacturing techniques.

2.2. Fuel Cell Technology

Fuel cell technology is a promising candidate to assist for transforming hydrocarbon-based economy towards hydrogen-inclusive economy (Kuang and Easler, 2007). A fuel cell is an electrochemical cell like a battery that converts chemical energy into electrical energy. All chemical energy is stored inside battery and after use it needs to charge again whereas fuel cell produces electricity continuously as long as fuel is fed. Therefore unlike battery systems, fuel cell does not require recharging. It converts hydrogen or hydrogen-containing fuel (natural gas or methanol) energy directly into electrical energy, producing heat and water as by-products and without involving combustion process.

Due to the characteristic of direct conversion of fuel energy into electricity, fuel cells are much efficient than conventional heat engines varying from 40% to 65% according to type of fuel cell. Fuel cell efficiency is limitedly dependent on power plant size. Having no moving parts inside fuel cell and a very few moving parts in the fuel cell systems give promise to higher reliability. It has also very little noise compared to internal combustion engines and gas turbines. No ash or large volume wastes are generated from fuel cell operation. However, the fuel cell power plant only produces CO_2 emissions if fossil fuels are used as hydrogen production source. Despite these benefits, the most significant challenges today are high cost, low durability and availability of hydrogen and hydrogen infrastructure (Basu, 2007).

First fuel cell (1839) was discovered by British Sir William Robert Grove (1811-1896) during electrolysis experiment. During his research, he comprehended that the opposite reaction of water electrolysis must be capable of production of electricity. He disconnected the battery from electrolyser and connected to electrodes together, observing current flow in the opposite direction, consuming hydrogen and oxygen gases. He called this device a ‘gas battery’ and it consisted of platinum electrodes placed in test tubes of hydrogen and oxygen, immersed in a bath of dilute sulfuric acid. However due to corrosion problems and materials instability, Grove’s fuel cell was not practical. At the beginning of 20th century, by Francis Bacon, a chemical engineer at Cambridge University, significant work on fuel cells began again. In 1950s Bacon first developed practical fuel cells that was based on alkaline (molten KOH) electrolyte and porous nickel electrodes. His work was licensed and used in the Apollo spacecraft fuel cells.

The fuel cell power plant for the Apollo spacecraft could supply 1.5 kilowatts of continuous electrical power with over 10000 hours of working operations (Rayment and Sherwin, 2003).

The basic physical structure of all fuel cell types consists of bipolar plates, gas diffusion layer (GDL), anode catalyst layer, solid or liquid electrolyte, cathode catalyst layer, gas diffusion layer, bipolar gas plates in turn and gaskets are used for preventing leakage of gases between anode and cathode. The anode and cathode consist of porous gas diffusion layers, usually made of highly electron conductive materials (porous thin carbon papers) so that the penetration of hydrogen or hydrogen-contained substances and oxygen is easily occurred from gas plates towards electrolyte. The charge carriers through electrolyte (from anode to the cathode or vice versa) are different depending on the type of fuel cells. The bipolar plates provide distribution of gases and collection of currents for external circuit in the fuel cell stack that is constructed by many individual fuel cells connected in series to yield the desired power. Figure 2.1 depicts the hydrogen/oxygen cell structure (Yuan et al., 2009).

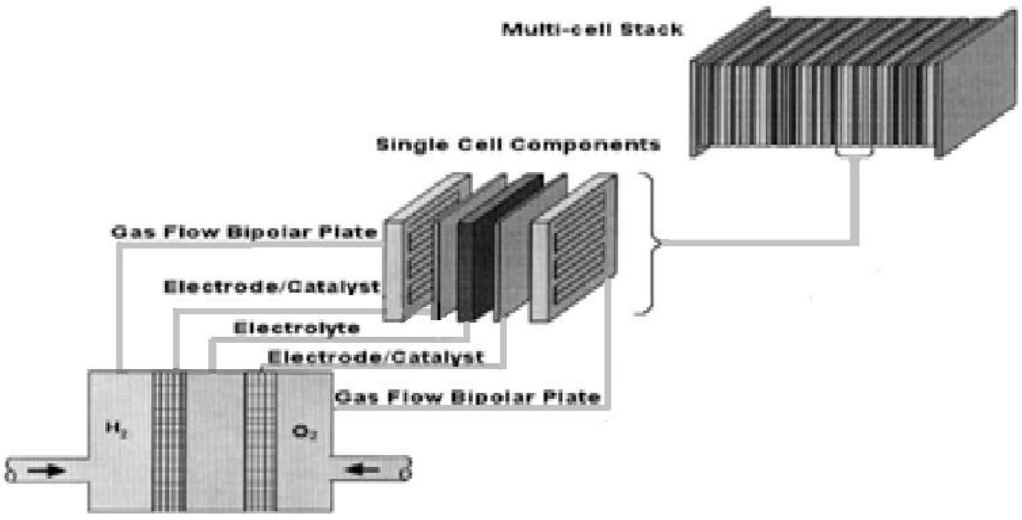

Figure 2.1. Basic structure of fuel cell

The anode reaction is either direct oxidation of hydrogen or methanol or indirect oxidation via a reforming step from hydrocarbon fuels. The cathode reaction is oxygen reduction from air for most fuel cells. For hydrogen/oxygen fuel cell, hydrogen fuel is supplied to the anode and split into an electron and a proton. Each takes a different path

towards the cathode. The electrons travel through external circuit producing direct current for a given load and then connects to the cathode, while protons pass through the ion permeable electrolyte to the cathode where they recombine with circulated electrons and produce water and heat as by-products. Direct current (DC) can be transformed to alternating current (AC) by an inverter. The external circuit can involve electric motors, lighting systems or other electrical devices as a load. Figure 2.2 shows hydrogen/oxygen fuel cell mechanism (Leon, 2008).

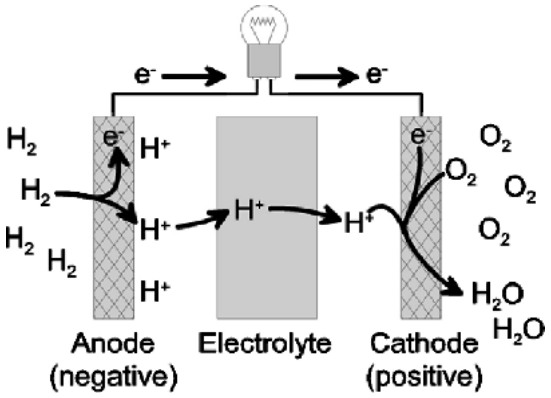

Figure 2.2. H_2/O_2 single fuel cell picture

In order to obtain an electrical current, electrolyte which is either a liquid or solid depending on cell types should separate these two half-reactions and be merely a good ion conductor and an electron insulator to avoid short circuit. Both H_2 oxidation and O_2 reduction reactions are very slow processes, catalysts are required to harness these reactions in a convenient way. The best catalyst is platinum for low temperature fuel cells that is expensive and limited on Earth and nickel is generally used for high temperature fuel cells.

Fuel cells (FCs) are basically classified into five groups mainly grouped after the electrolyte type; solid oxide fuel cell (SOFC), polymer electrolyte membrane fuel cell (PEMFC), alkaline fuel cell (AFC), phosphoric acid fuel cell (PAFC), molten carbonate fuel cell (MCFC). Besides, there is one more fuel cell type as direct methanol fuel cell (DMFC) which is distinguished according to fuel type but the operation method and material inside the cell are almost same with PEMFC. However they also involve other important differences such as materials of construction, the fabrication techniques, and the system requirements (Holland et al., 2007).

Solid Oxide (SOFC) operates between 500-1000°C and the electrolyte is a solid, nonporous metal oxide that is impermeable to gas crossover from one electrode to other. The charge carriers are oxygen ions. Due to the high operation temperature, high reaction rates are achieved without the need of expensive catalysts and if natural gas is used as a fuel, there is no need to fuel reforming because of internally reformation. The use of solid electrolyte reduces hardware corrosion and management problems. However high temperature enhances the breakdown of cell components and the ceramic solid electrolyte lowers the performance due to relatively low conductivity.

Polymer Electrolyte Membrane (PEMFC) type of fuel cell operates relatively at low temperatures between 50-100 °C and the electrolyte is a solid organic polymer membrane used to conduct protons. Advantages due to the solid electrolyte use are the same with SOFC systems. Quick start-up and high current densities benefits are achieved. However low temperature operation requires expensive catalysts (largely platinum) to increase the chemical reaction rates. Heat and water management balance are not easily handled in a practical system and high sensitivity to fuel impurities is another problem.

Alkaline (AFC) process temperature is between 50-250°C and the electrolyte is an aqueous solution of potassium hydroxide (KOH) as either mobile or soaked inside a matrix and wide range of electrocatalysts can be used (e.g. nickel, silver, metal oxides). It has an excellent performance with hydrogen and oxygen compared to other candidate types. Because of high CO_2 and CO poisoning, the reformed fuel with air is not suitable.

Phosphoric Acid (PAFC) operates at around 200 °C and aqueous solution of phosphoric acid soaked in a matrix is an electrolyte in this type of cell. The electro-catalyst in both side is platinum. The higher temperature operation has the benefit of cogeneration of electricity and heat. Removal of CO_2 is expensive.

Molten Carbonate (MCFC) operation temperature is around 600 °C and the electrolyte is the combination of alkali carbonates retained in a ceramic matrix. Nickel for anode electrode and nickel oxide for cathode are adequate to speed up reactions. Noble metals are not preferred due to high reaction rates and natural gases can internally be reformed without separate part like SOFC. However electrolyte is highly corrosive that reduces the fuel cell durability.

The most prevalent fuel cell type is the PEM type fuel cell owned to the largest amount of publications and patents but for stationary power applications (>250 kW), high temperature fuel cells (SOFC and MCFC) have important advantage and for portable applications (up to 1 kW) direct methanol fuel cells (DMFC) will be introduced commercially due to hydrogen storage problems in small sizes. The polymer electrolyte membrane (PEM) fuel cell technology has drawn the most attention especially in transportation applications due to its high efficiency, compact, lightweight, simple units without moving parts, quick start-up, load following capabilities, modularity and versatility (Barbir, 2005). The achievable efficiency of such systems is around 40-60%.

2.2.1. Polymer Electrolyte Membrane Fuel Cell

The PEMFC uses a polymer membrane as its electrolyte which is an electronic insulator, but an excellent hydrogen ions conductor. The membrane material consists of a fluorocarbon polymer backbone, similar to Teflon, to which sulfonic acid groups are attached. These acid molecules are fixed to the polymer but the protons on these acid groups are free to migrate along the membrane. Platinum or platinum alloys in nanometer size particles are the electro-catalysts. The anode and cathode are prepared by applying a small amount of platinum black to the surface of a thin sheet of a porous, carbon layer. The anode-electrolyte-cathode assembly is referred to as Membrane Electrode Assemblies (MEAs), with only a few hundred micron thickness. The thermal management in the cells and water management in the MEAs are critical points for efficient operation of PEMFC. Because the water presence is necessary to conduct protons effectively through the membrane therefore the operation temperature of the PEMFC is limited to avoid the water vaporization. The anode and cathode are contacted on the back side by flow field plates made of graphite. The ridges between the channels make electrical contact and conduct current to the external circuit and through the channels simultaneously fuel supply to anode and oxidant supply to cathode are provided. The mechanism of this kind of fuel cell is explained as hydrogen/oxygen fuel cell in section 2.2.2. The basic hydrogen/oxygen (air) fuel cell electrochemical reactions at both anode and cathode side and the overall reaction are given as below;

Anode reaction : $H_2 \rightarrow 2H^+ + 2e^-$

Cathode reaction : $\frac{1}{2} O_2 + 2H^+ + 2e^- \rightarrow H_2 O$

Overall reaction : $H_2 + \frac{1}{2} O_2 \rightarrow H_2 O$

The maximum amount of electrical energy generated in a fuel cell corresponds to change in Gibbs free energy ΔG that means energy available for external work.

$$W_e = -\Delta G \tag{2.1}$$

It is evaluated by the difference between free energy of the product and free energy of the reactants. The concept of electrical work is similar to the moving of an electron through a circuit. The energy required to move a given charge is given as;

$$W_e = zFE = \left(\frac{eq\ electrons}{mol\ reactant}\right)\left(\frac{coulombs}{eq\ electrons}\right)\left(\frac{joule}{coulombs}\right) \tag{2.2}$$

In equation (2.2) symbol E expresses a voltage based on the concept of electromotive force. Combining both equations, an expression for the maximum possible reversible voltage of an electrochemical cell can be deduced as ;

$$E^0 = -\frac{\Delta G}{zF} \tag{2.3}$$

for 1 mole oxidized fuel without any irreversible losses. Since F is Faraday constant (96487 C) and z is the electron transfer number as constants, the functional dependence of the maximum possible voltage is related only the dependencies of the Gibbs free energy such as temperature and pressure of the reactants and products (Mench, 2008). Therefore, for a given temperature, pressure and set of species' concentrations, thermodynamics can determine the maximum possible (ideal) voltage that a fuel cell can theoretically produce. The fuel cell ideal thermodynamic electrical potential at 25° C and 1 atm pressure is calculated as 1.23 V.

When a fuel cell is fed by reactant gases, but without any electrical circuit, it will not generate any current and in this case, hypothetically it is expected that the cell potential would be equal to the theoretical cell potentials at given conditions

(temperature, pressure and concentration of reactants). However, practically, this potential, named as the open circuit potential, is slightly lower than the theoretical potential, generally less than 1 V. This elucidates that there are some losses in the fuel cell even when there is no external current generated. When the electrical current is circulated with a load (such as a resistor) from outside the fuel cell, the open circuit potential is decreasing even more as a function of current or current density due to irreversible losses (Barbir, 2008).

Determination of irreversible losses of a PEM fuel cell is essential to evaluate its performance in terms of cell voltage, current density and power. These losses are called overpotentials or polarizations hence the voltage versus current graph as shown the performance characteristic of a fuel cell is called polarization curve. The losses could be generated primarily from three sources as activation, ohmic and concentration over potentials. Activation losses are associated with the slowness of the reactions taking place on the surface of electrodes. Ohmic losses are caused by the resistance of the membrane to the flow of migrating ions during an electrochemical process. The mass transport or concentration losses occur due to concentration gradients of the reactants at the electrode surface due to a rapid consumption especially at higher currents or current density values (Kazım, 2004). Losses and their effective regions over the current density are clearly observed from current density versus voltage curve as shown at Figure 2.3.

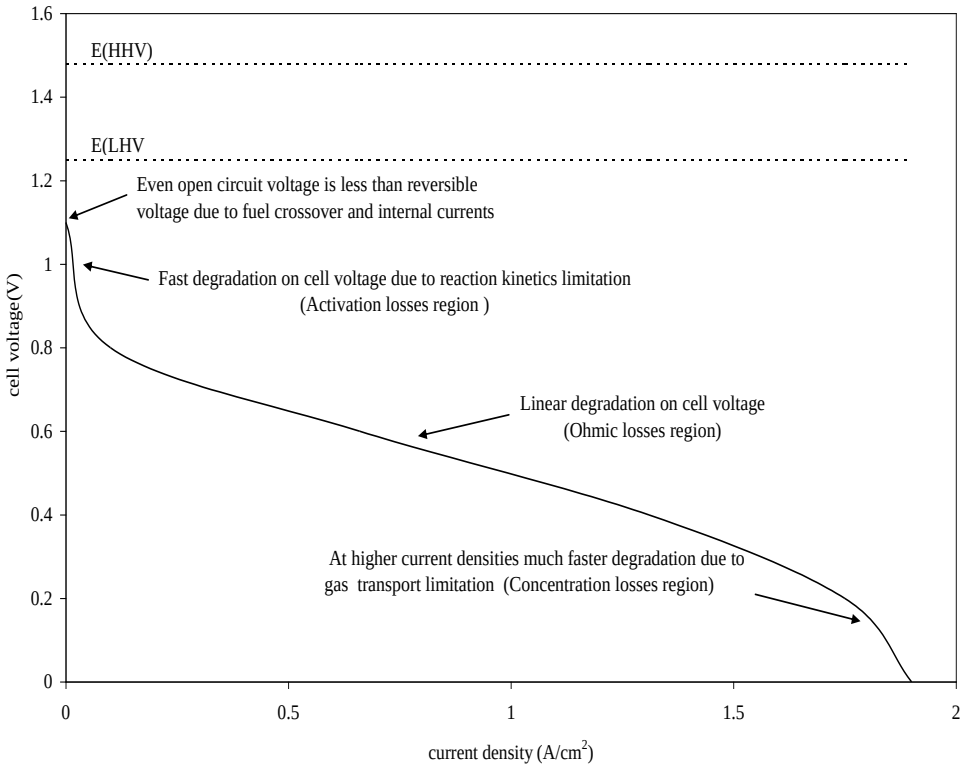

Figure 2.3. Voltage versus current density polarization curve

These losses increase when more current is acquiring from the fuel cell that means when the more current is generated, the output voltage falls. Therefore, the fuel cell voltage output can be described by the following equation:

$$E = E_{rev} - \left(V_{act,a} + V_{act,c}\right) - V_{ohmic} - \left(V_{conc,a} + V_{conc,c}\right) \quad (2.4)$$

where E is the real output voltage, E_{rev} is the thermodynamically calculated reversible voltage, $V_{act,a}$ and $V_{act,c}$ are the activation losses on the anode and cathode electrode, respectively, generated at low current densities due to reaction kinetics, V_{ohmic} is the ohmic loss, dominant at medium scale current densities, $V_{con,a}$ and $V_{con,c}$ are the concentration losses on the anode and cathode, related to consumed concentration of reactants at the electrode surface by the effect of high current densities.

The pressure and the concentration of the reactants affect the Gibbs free energy and thus the thermodynamic voltage. This is given by the Nernst equation,

$$E_{rev} = E^0 + \frac{RT}{zF} In(P_{H2}^* \, (P_{O2}^*)^{0.5}) \quad (2.5)$$

where z is equal to 2 as the electron transfer number for 1 mol hydrogen molecule in the fuel cell reaction; R is the universal gas constant with the value of 8.314 J/(molK); T is the fuel cell operation temperature (K); P_{H2}^* and P_{O2}^* denote the partial pressures of hydrogen and oxygen at the catalytic interface of the anode and cathode, respectively, and E^0 denotes the reversible open circuit voltage at standard pressure. The standard state defines a standard state reference potential ${E_O}^0$ (equal to 1.229 V at 298.15 K and 1 atm) and $E°$ changes from the standard state reference potential (${E_O}^0$) dependent on the temperature change.

$$E^0 = {E_O}^0 + (T - T_O)(\frac{\Delta S°}{zF}) \quad (2.6)$$

where the entropy change of a given reaction is approximately constant. When the literature values for the standard-state entropy change is used, the above equation can be rewritten as the function of temperature (Moreira and Da Silva, 2009) ;

$$E^0 = 1.229 - 0.85 \times 10^{-3} \times (T - 298.15) \quad (2.7)$$

After substituting equation (2.7) into general Nernst equation (2.5), thermodynamic equilibrium potential equation depends on the cell temperature and the anode and cathode partial pressures are as follows ;

$$E_{rev} = 1.299 - 0.85 \times 10^{-3} \times (T - 298.15) + 4.3 \times T \left[In(P_{H2}^*) + \frac{1}{2} In \, (P_{O2}^*) \right] \quad (2.8)$$

The derivation of hydrogen and oxygen partial pressures at the anode and cathode catalytic interface, in turn, is based on Maxwell-Stefan equations and the partial pressures at the catalytic surface are assumed to be same across the entire cell. The partial pressure of hydrogen depends on the water content in the anode channel as follows;

$$P_{H2}^{*} = (0.5\ P_{H2O}^{sat}) \left[\frac{1}{exp\left(\frac{1.653 \times i}{T^{1.334}}\right)\ X_{H2O}^{anode}} - 1 \right] \tag{2.9}$$

The partial pressure of oxygen at the water-gas interface is related to the water concentration at the cathode channel (Amphlett J.C. et al., 1995) ;

$$P_{O2}^{*} = (P_{H2O}^{sat}) \left[\frac{1}{exp\left(\frac{4.192 \times i}{T^{1.334}}\right) X_{H2O}^{cathode}} - 1 \right] \tag{2.10}$$

The molar fraction of saturated water in a gas stream for a given temperature is given by (Dong et al., 2006) and assuming that for the cathode side the effective cathode water pressure is equal to the saturation pressure of water vapor at temperature T ;

$$X_{H2O}^{cathode} = \frac{P_{H2O}^{sat}}{P_{cathode}} \tag{2.11}$$

Assuming that the fuel gas is pure H_2 humidified with water vapor and the effective anode vapor pressure of water is half of the saturated water pressure. Hence the molar fraction of water at saturation at the anode electrode side;

$$X_{H2O}^{anode} = \frac{0.5\ P_{H2O}^{sat}}{P_{anode}} \tag{2.12}$$

The saturation pressure of water vapor (in bar) dependent on temperature can be computed from (Berning and Djilali, 2003) by using the following expression ;

$$\log P_{H2O}^{sat} = -2.1794 + 0.02953(T - 273.15) - 9.1837 \times 10^{-5}(T - 273.15)^2 + 1.4454\ \times 10^{-7}(T - 273.15)^3 \tag{2.13}$$

When a graph of activation overvoltage against logarithm of current density is plotted, the graph approximates to a straight line. This behavior is observed by Tafel. Therefore, the equation that describes the overvoltage of the electrochemical reaction is called Tafel equation and this equation is only valid when $i > i_o$.

$$\Delta V_{act} = \frac{RT}{z\alpha F} In \frac{i}{i_o} \quad (2.14)$$

The constant α is called charge transfer coefficient and it depends on the symmetry of the activation barrier and defines how the change in the electrical potential across the reaction interface changes the sizes of the forward versus reverse activation barrier. For 'symmetric' reactions α is equal to 0.5. For most electrochemical reaction, α changes from 0.2 to 0.5. Exchange current density, i_o, is the current density at which the activation overvoltage starts to move from zero ($i_0 = i, @\ \Delta V_{act} = 0$. At equilibrium conditions it seems that there is no activity and no electron transfer from or to the electrode however it is not true, in this case, there is also the reverse reaction taking place at the same rate. This difference of backwards and forwards current density is called 'exchange' current density, i_o. The higher i_o value gives the faster reaction. Therefore it is vital to make its value as high as possible to improve the fuel cell performance by decreasing activation losses. In fact, any increase in i_o with temperature has much greater affect than increase in α. The key parameter for the activation overvoltage can be considered as i_o than α. In a PEM fuel cell, the value of exchange current density at the cathode electrode is relatively low compared to value at the anode electrode. As an example, typical value for i_o could be 0.1 $mAcm^{-2}$ at the cathode and 200 $mAcm^{-2}$ at the anode. Consequently the activation voltage drop can be predominantly attributed to the cathode reaction. Tafel equation can be rearranged according to current density by Butler-Vollmer equation that is correlated to reaction kinetics (Larminie and Dicks, 2003).

$$i = i_o \exp\left(\frac{z\alpha F \Delta V_{act}}{RT}\right) \quad (2.15)$$

Ohmic losses is simply proportional to the current density. These kind of losses occur due to the resistance to electron flow in the electrodes and graphite collector plates and ion flow in the electrolyte. The ion resistance inside the electrolyte is usually dominant irreversibility. In order to reduce the ohmic losses, thinner membrane could be used to facilitate the ion flow however in this case, mechanical strength problem of membrane could be formed. Therefore the balance thickness of the membrane is a

critical issue to improve cell performance significantly. The ohmic overvoltage can be expressed according to Ohm's Law (Mann et al., 2000);

$$\Delta V_{ohm} = i \times (R_{electronic} + R_{int}) \tag{2.16}$$

where $R_{electronic}$ is difficult to measure or predict and assumed to be inconsequential in comparison to the R_{int} and thus it is ignored. The term R_{int} is a complex function of water content and distribution in the membrane. A general expression for the ohmic resistance of the electrolyte is given by (Mann et al., 2000);

$$R_{int} = \frac{r_M L}{A} \tag{2.17}$$

where r_M is the membrane-specific resistivity for the flow of hydrated protons (ohm cm), L is the thickness of membrane (cm) and A is the active surface area of cell (cm^2). The Nafion membrane manufactured by the Dupont is widely used in PEM fuel cells and Dupont classifies membranes according to their thickness as;

- Nafion 117: 7 mil (L=178 μm) ;
- Nafion 115:5 mil (L=127μm);
- Nafion 112:2 mil (L=51 μm)

Thickness and the active cell area are the known parameters for specific cell however it is impossible to describe r_M theoretically , thus the following semi-empirical equation has been derived (Mann et al., 2000) as a function of cell current density and temperature.

$$r_M = \frac{181.6\left[1+0.03(i)+0.062\left(\frac{T}{303}\right)^2 i^{2.5}\right]}{[\lambda-0.634-3i]\times e^{4.18\left(\frac{T-303}{T}\right)}} \tag{2.18}$$

where λ is an adjustable fitting parameter with a possible maximum value 23 and usually assigned a value between 10 and 20 (Fowler et al., 2002). This value is effected by the preparation procedure of the membrane and is a function of relative humidity and stoichiometric ratio of the anode gas. The parameter λ has been introduced by (Springer

et al., 1991) and express the number of sulfonic group SO_3^- in the membrane that provides the proton transfer through membrane. Under the ideal condition of 100% relative humidity, it has a value of 14. There are also reported values in the order of 22 and 23 under oversaturated conditions (Mo et al., 2006).

Concentration losses are caused by mass diffusion limitations on the availability of the reactants from the flow channels to the reaction catalyst sites causing the decrease of the partial pressures of the hydrogen and oxygen gases. The electrode reactions require a constant supply of reactants in order to maintain the current flow. When the diffusion limitations occur, part of the available energy is used to drive the mass transfer, decreasing the output voltage. Similar problems can generate if a reaction product water accumulates around the electrode surface and hinders the diffusion paths or dilutes the reactants (Al-Baghdadi, 2005). The reduction in gas partial pressure causes a reduction in voltage. The electrochemical reaction potential changes with hydrogen partial pressure and this relationship is given by Nernst equation (Barbir, 2008) in terms of concentration gradients;

$$\Delta V_{diff} = \frac{RT}{zF} In(\frac{C_B}{C_S}) \tag{2.19}$$

where C_B is the bulk concentration of reactant and C_S is the concentration of the reactant at the catalyst surface. According to Fick's Law, the flux of reactant is proportional to concentration gradient;

$$J = \frac{D(C_B - C_S)}{\delta} A \tag{2.20}$$

In steady state, the rate at which the reactant species is consumed in the electrochemical reaction is equal to the diffusion flux. In terms of Faraday Law;

$$J = \frac{I}{zF} \tag{2.21}$$

By combining equation (2.20) and (2.21), the following equation is achieved and i is the current density obtained dividing current (I) to active cell area (A);

$$i = \frac{zFD(C_B - C_S)}{x} \tag{2.22}$$

According to this relation, the reaction concentration at the catalyst surface depends on the current density means that the higher the current density, the lower the surface concentration. The surface concentration is equal to zero when the rate of consumption exceeds the diffusion rate so the reactant is consumed faster than it comes the surface. In the limiting case of mass transport where the reactants' concentrations at the catalyst surface sites are zero, the current is called the limiting current density (i_L). The limiting current density is the maximum current density drawn from the cell that the fuel is run out at a rate with the maximum supply speed. The current density cannot excess this value because the fuel gas can not be fed at a greater rate. Therefore for $C_S = 0$, $i = i_L$ and the limiting current density is written by;

$$i_L = \frac{zFDC_B}{x} \tag{2.23}$$

By combining equation (2.19), (2.22), (2.23), a relationship for concentration overvoltage is obtained as;

$$\Delta V_{diff} = \frac{RT}{zF} In\left(1 - \frac{i}{i_L}\right) \tag{2.24}$$

Another approach is entirely empirical and expressed as an exponential function of the current densities (Kim et al., 1995);

$$\Delta V_{diff} = m \times exp(ni) \tag{2.25}$$

where m and n are parameters that have to be evaluated experimentally and the values are about $3 \times 10^{-5}\ V$ and 8×10^{-3} cm^2/mA in turn (Xia and Chan, 2007).

CHAPTER 3

LITERATURE SURVEY ON MODEL DEVELOPMENT

The performance of a PEM fuel cell can be expressed simply through the analytical formulation of the polarization curve as mentioned in Chapter 2. Mathematical models and simulation are required as tools for design optimization of fuel cells, stacks, and fuel cell power systems. To understand and improve the steady-state performance of PEMFCs, researchers have developed several different mathematical models to predict the behavior of voltage variation with the discharge current. In the literature, the studies were classified mainly into two modeling approaches. The first approach comprises mechanistic models based on thermodynamic, fluid mechanics and electrochemical equations (Yi and Van Nguyen, 1999; Bernardi and Verbrugge, 1992; Springer et al., 1991, Rowe and Li, 2001). In these models, knowledge of not readily available model parameters such as transfer coefficients, humidity levels, membrane, electrode and active catalyst layer thicknesses etc. is essential. Because their values inside the cell are modified by gradients of temperature, pressure and humidity, by physical constraints and by current density. On the other hand, the second approach includes empirical modeling that are easier to be obtained than mechanistic models and are generally accurate over a small operating range. This models are applied to predict the input parameters and issues affecting on the voltage–current characteristics of the fuel cell without any knowledge of the physical and electrochemical phenomena involved in fuel cell operation. They fail to show the actual processes generated in fuel cell operation thus are not applicable over a broad range of conditions. An approach combining both mechanistic and empirical modeling techniques called as semi-empirical modeling has the potential to supply both mechanistic validity and the inherent simplicity of the empirical models. The basic non-mechanistic term is the ohmic overvoltage in this model that is primarily empirically based. A brief overview on semi-empirical models proposed in the literature started with Amphlett et al. (1995) presented a model for the fuel cells manufactured by Ballard Power Systems of Burnaby, BC, Canada. The model was derived from a mechanistic model which was used to provide the structure of the equations and then the parameters

of these equations where found by using regression techniques to fit the experimental data. This steady state electrochemical model had both mechanistic and empirical features but was restricted for applications of two particular cells as Ballard Mark IV and Mark V (Mann et al., 2000). This model was further improved by Fowler et al., 2002. The commomly used models are given as follows;

The Fuel Cell Handbook model provides a physical steady state model involving activation, ohmic and concentration polarizations. The polarizations are clearly associated with each electrode and the cell voltage is given as a difference between the electrode potentials. Considering that the polarizations at the electrodes can be given together the model is as follows;

$$E = \Delta E_{rev} - \frac{RT}{\alpha zF} In\left(\frac{i}{i_0}\right) - iR_{int} + \frac{RT}{zF} In\left(1 - \frac{i}{i_L}\right) \quad (3.1)$$

where ΔE is the difference between ideal reversible potential of cathode and anode. For fuel cell stack , all the terms in equation are multiplied by the number of cells inside the stack. This model is written in terms of current density so the R_{int} is an area-specific resistance.

Kim et al.'s model (1995) physically based activation and ohmic polarization terms are as proposed first. The structure of the rest between model and the experimental observations was found to be exponential and empirical exponential term was added. Thus this model structure is semi-empirical derived one.

$$E = E_0 - blog(i) - iR_{int} - mexp(ni) \quad (3.2)$$

$$E_0 = E_{rev} + b\ log(i_o) \quad (3.3)$$

Amphlett et al's (1995) semi-empirical model is proposed for the Ballard Mark IV PEM fuel cell and composed of thermodynamic potential, activation overvoltage and ohmic overvoltage.

$$E = E_{reversible} + V_{act} + V_{ohm} \quad (3.4)$$

$$V_{act} = \varepsilon_1 + \varepsilon_2 + \varepsilon_3 TIn(C_{O2}) + \varepsilon_4 TIn(I) \quad (3.5)$$

$$V_{ohmic} = -IR_{int} = -I(\varepsilon_5 + \varepsilon_6 T_{stack} + \varepsilon_7 I) \quad (3.6)$$

where ε values are parametric coefficients based on the experimental data that depends on the stack and I is used as current instead of current density and C_{O2} is the oxygen concentration. In this model, oxygen concentration at the catalyst interface has also influence on the activation losses (Pasricha et al., 2007).

No matter what kind of models is used, there should be some errors between the model and the actual experimental data of the PEMFC because of the assumptions and approximations in the model. In order to increase the accuracy of the models and to reflect the actual PEMFC performance better, it is essential to optimize the parameters of the models. A sum of the squares of the errors between the model output voltage of the PEM fuel cell stack and the experimental output voltage of the actual PEM fuel cell stack can be observed as an objective function for optimization to determine these model parameters;

$$\min\left(y = \sum_{k=1}^{k}\left(E_{experimenal} - E_{model}\right)^2\right) \quad (3.7)$$

where y is the objective function, $E_{experimental}$ is the experimental stack voltage, E_{model} is the model output voltage, k is the number of the experimental data point.

Nonlinear regression is applied to determine the model parameters. Regression analysis is the application of the mathematical and statistical methods for analyzing the experimental data and fitting the mathematical models to the data by the prediction of the unknown parameters of the models. The common way of non-linear regression is the least squares method. Many least squares algorithms are available for non-linear parameter estimation. Three of them are the steepest descent algorithm, the Gauss-Newton algorithm and the Levenberg-Marquardt algorithm (LMA). The steepest-descent method has the advantage that the sum of the squared residuals reach to its minimum without any diverging. However it has the disadvantage of slow convergence when the sum of the squared residuals approaches its minimum. The other method, Gauss–Newton has the advantage of fast convergence when the sum of squared residuals gets closer to its minimum but has the disadvantage of diverging if the initial guesses of all the parameters are not close enough to their final iterated values. The

Marquardt method is an interpolation technique between the Gauss-Newton and the steepest descent methods (Xia and Chan, 2007) and more robust than Gauss-Newton means that it finds a solution even if it starts very far off the minimum. The LMA is a very popular curve-fitting algorithm used in many software applications for solving curve-fitting problems.

CHAPTER 4

EXPERIMENTAL SETUP AND PROCEDURE

Although fuel cells can be considered as an alternative way to support the sustainability, security of supply and economical competitiveness for energy challenge, the technology is not mature yet enough for wide range applications and needs to be further improved. In order to evaluate the improvements in fuel cells, common agreed measures for system power density, efficiency, dynamic behavior and durability are strongly required. The harmonized, validated and benchmarked testing procedures for all fuel cell systems as well as system components provide a common agreed basis to the wide variety of boundary conditions caused by different applications, stack technologies, types of fuels, fuel quality. These harmonized testing procedures are even necessary for the relatively simple and widely used polarization curve tests. To create a common sense among different institutions performing fuel cell tests, several international activities have been started to set up testing procedures with the aim of transparent and objective interpretation of the results.

Within the Fifth Framework Programme (FP5), The European Commission financed the Thematic Network FCTESTNET which included 55 European partners for harmonizing fuel cell testing procedures. As a follow-up of FCTESTNET within the Sixth Framework Programme (FP6), the project Fuel Cell Testing, Safety and Quality Assurance ($FCTES^{QA}$) provides experimental validation of the testing procedures described in FCTESNET. The experimental study proposed in this thesis have been employed in the framework of FCTESTNET and $FCTES^{QA}$. At Joint Research Centre (JRC), Institute for Energy (IE), a fuel cell testing facility was set up in 2005. The main objective of the testing facility is to compose an European Commission (EC) reference laboratory for fuel cell performance with a contribution of scientific community and industry. The facility supports the development of regulations, codes and standards (RCS) within the European Hydrogen Platform (HFP) in the frame of the International Partnership for the Hydrogen Economy (IPHE).

The testing procedures called Test Modules are originally developed under the Research&Training Network (RTN) FCTESTNET (Fuel Cells Testing &

Standardisation NETwork). Test module TM PEMFC ST 5-3 used in this study is entitled *'Testing the voltage and the power as a function of the current density (Polarization curve for a PEMFC stack)'*.

The purpose of the Test Module TM PEMFC ST 5-3 is to characterize the performance of a (water cooled) PEMFC power stack under constant current conditions. The primarily test outputs are the measured stack voltage and the calculated power. Other test outputs are not mandated but recommended. These are the measurement of the voltages of the individual cells in the stack, the stack (or coolant outlet) temperature, the outlet temperatures of the reactants (fuel and oxidant), the pressure drops of the stack fluids (coolant and reactants) and the electrical and thermal stack efficiencies. Polarization curves are often baseline measurements to qualify PEMFC stacks and components (e.g. catalyst, membrane and electrode materials, membrane electrode assemblies, bipolar plates etc) in a given application or for particular test conditions.

Eventually, these experimentally validated procedures form part of international standards prepared by the International Electrotechnical Committee (IEC). Such standards allow to establish and to compare in a harmonized way the performance of various kind of PEMFC power stacks under different boundary and operation conditions and to evaluate improvements in PEMFC materials, components and technology development. In this way, the harmonized testing procedures contribute to the early and market-oriented development of PEMFC technology.

4.1. Test Objective

The main objective of this test is to assess the performance of a 10 kW power stack. The result of the test could be compared with the output result of other tests execute at JRC or in other laboratory. The stack of 10 kW peak power used in this test is owned by the JRC.

4.2. Test Object Description

Table 4.1 and 4.2 provide detailed information about the stack parts and components. However some information are proprietary.

Table 4.1. Details of the used stack

Stack manufacturer	Nedstack
Fuel cell technology	PEMFC
Stack model	10 kW peak power stack
Number of cells	75
Stack dimension	264×550×188 mm^3
Stack weight (kg)	37
Stack nominal power (W)	9500
Stack peak power (W)	10000
Stack voltage range (V)	75 at OCV
Lowest stack voltage allowed (V)	15
Lowest cell voltage allowed (mV)	200
Fuel dead end	No
Pressure difference allowed between anode and cathode (kPa)	<30

Fuel cell stack components, material and coating of the bipolar plates, gasket type and thickness and clamping force are all proprietary information. In addition, the specifications of fuel cell components such as MEA assembling, anode and cathode Pt catalyst loading (mg/cm^2) , electrodes, thickness and type of gas diffusion layer, loading and composition of catalyst layers and type and thickness of membrane are also proprietary information. Therefore we have no information about these properties. Figure 4.1 depicts the PEMFC stack used for the tests.

Table 4.2. Details of the stack components

Fuel cell : flow field design	Parallel
Fuel cell : active geometric area (cm^2)	200
Stack technology (collectors)	Graphite
Heating /cooling system	De-ionised water
Minimum flow of the coolant (lpm)	2.75

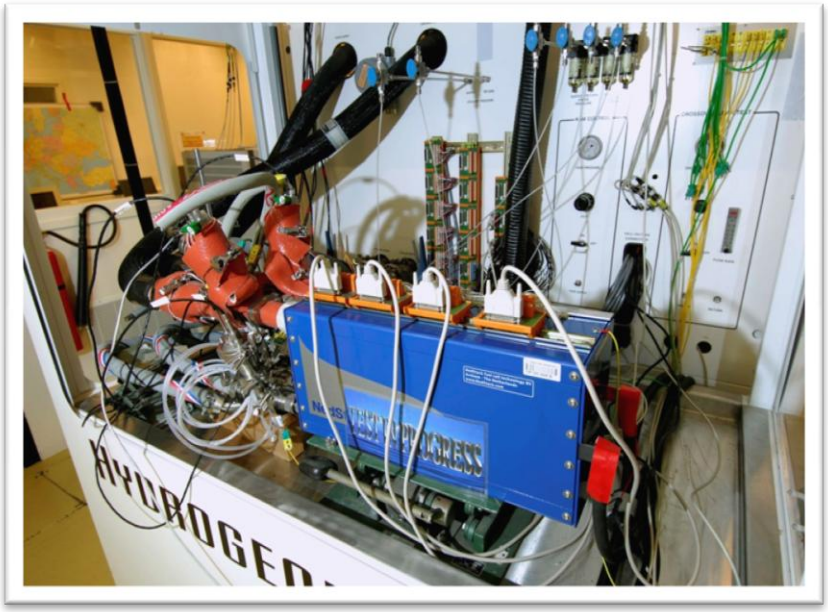

Figure 4.1. 10 kW peak power proton exchange membrane fuel cell (PEMFC) stack

4.3. Description of the Test Setup

The test is performed using the test equipment FCATS HS Series 100 kW model produced by Hydrogenics Corp., Canada as shown in Figure 4.2.

Figure 4.2. Up to 100 kW PEMFC power stack testing device (FCATS)

The test bench comprises sub-systems to provide fuel and oxidant to the stack in a defined manner (flow rate, pressure, temperature and relative humidity) and an electronic load to draw current/load from the stack and a coolant sub-system for controlling stack temperature. The test equipments are defined as follows;

- a PID (proportional –integral- derivative) regulated closed loop with an electric heater inside a tank reservoir, a pump and a water/water heat exchanger to provide de-ionized water as a stack coolant
- reactant gas circuitry made of stainless steel with 5 MFC (mass flow controller) of Brooks Instrument for the reactant gases at the fuel side of which one is used and with 4 MFC at the oxidant side of which three are used
- a water cooled electronic load, TDI Dynaload model WCL 488 400-1000 1200 to obtain current from the stack
- two cell voltage monitoring systems for a total of 400 cells
- a PLC (programmable logic controller) including a battery UPS (uninterrupted power supply) and a PC including operation & data acquisition software.

The waste heat generated by the fuel cell stack is removed by deionized water flowing inside the bipolar plates of stack. The heat dissipated by the stack coolant and other test ancillaries is removed via an externally supply of water using the principle of geothermal cooling. The setting of the coolant inlet temperature is carried out using a PID controller combined with a thermocouple placed at the stack inlet. Depending on the coolant outlet temperature either the flow of the externally supplied cooling water into the heat exchanger via a proportional valve or the power of the electrical heater in this circuit is adjusted to regulate the coolant inlet temperature. The deionized water used to cool the stack to a certain temperature or to heat it up during start-up is produced from tap water by reverse osmosis employing an ionomer membrane followed by a patented electro-deionization process. After process, the deionized water has an ionic conductivity of 0.1 $\mu S\ cm^{-1}$ and then is treated by ozone and ultraviolet radiation to prevent microbial contamination prior to its use.

The MFCs are connected to field point I/O interface modules of National Instruments operated via RS-232 communications by a PC using an operation and control-based Labview software. The H_2 MFC has a range of 0-1600 nlpm (normal litres per minute) and the air-flow rate is regulated by three MFCs each of 0-2200 nlpm

range. The PC software regulates the air flow by one MFC for up to 600 nlpm and by all three MFCs when this value is exceed. The flow rate accuracy is 1% of the full scale of the MFC. The uncertainty of the actual flow rate is thus depended on the MFC range employed.

The electricity generated during the tests can be dissipated through an external electrical load or can be connected to the institute electrical grid after power conditioning. At IE fuel cell testing facility, it is fed to the building grid of the laboratory using a 120-kVA dc/ac electronic load inverter.

The humidification of the reactant gases is provided by adjusting the dew point and gas temperatures of the reactants in three steps by one PID controller (combined with thermo couples) per stack reactant fluid. The first step is the saturation of the dry reactant gas at room temperature by mixing them with 180 °C hot steam, then second step is the quenching of the saturated gas mixture to the dew point temperature of the gas in condensing heat exchanger and removing the excess water via this heat exchanger and as final step the humid gas is re-heated to its gas temperature set point.

A schematic of a typical fuel cell test setup is shown in Figure 4.3. Appendix A provides details on the components and instrumentation used in the setup.

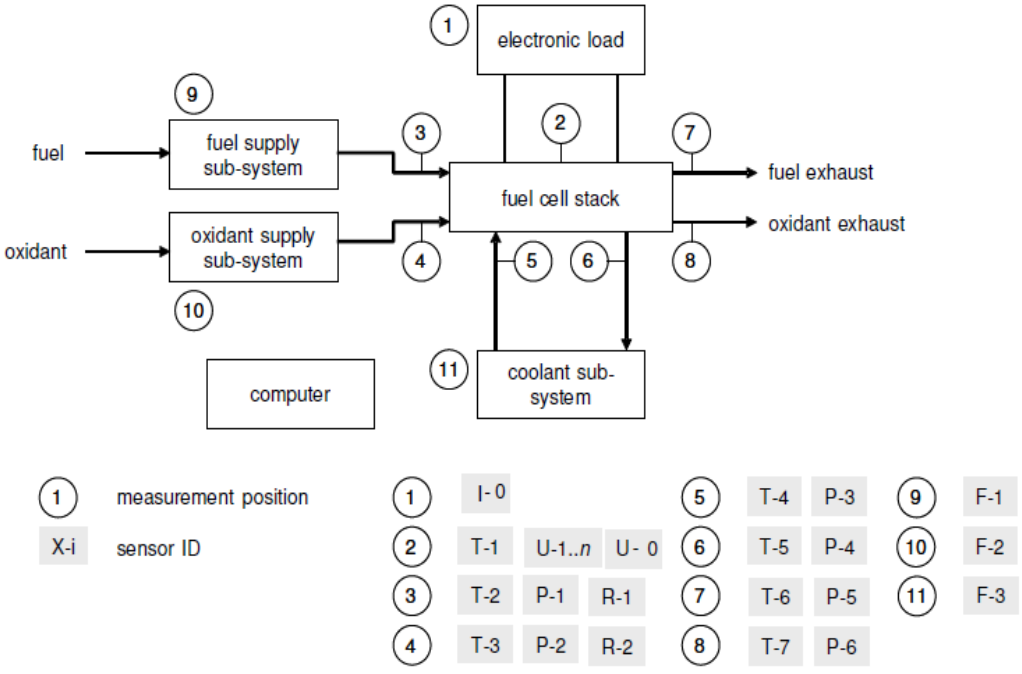

Figure 4.3. Test set-up with sub-systems and sensors and sensor locations

The location of the inlet and outlet stream connectors of the D shape stack and of the temperature and pressure sensors placed in the streams are shown in Figure 4.4.

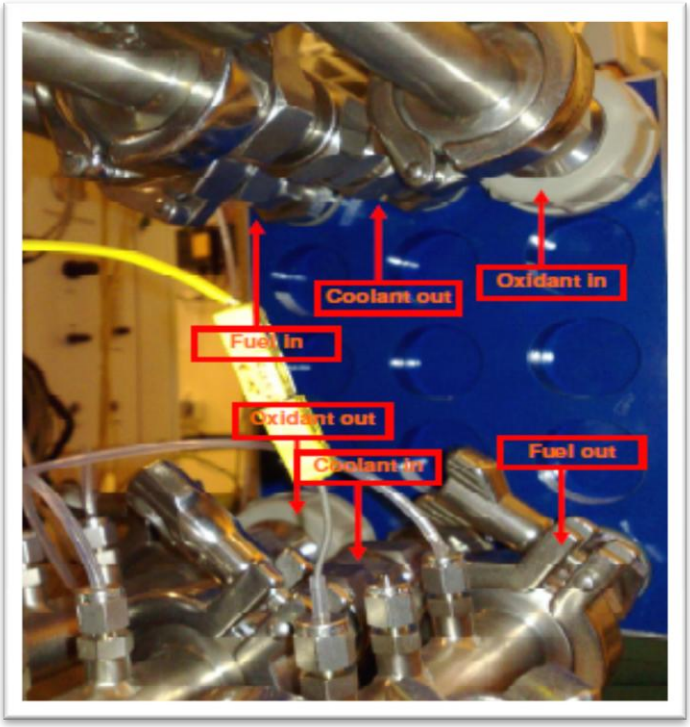

Figure 4.4. Photograph view of the tested stack and inlet and outlet streams of the stack

4.4. Test Facility Units & Auxiliaries

The operations within the Fuel Cell Test Facility are based around the testing of fuel cells under various environmental conditions such as temperature, humidity. Humidified air is provided to the fuel cell using a natural gas fired clean steam generator (CSG) combine with a normal water supply passed through a de-ionised water treatment (DIWT) plant. Hydrogen gas is the fuel source piped to the fuel cells. Currently, bottled hydrogen is directly supplied from a Gas Bottle Distribution Store. Control of the supply and removal of gases is generated via a Fuel Cell Automated Test Station (FCATS). Sampling and testing of gases is made by analysers in an Infrared Spectrum Analyser (ISA) Room to the rear of the FCATS room.

IE plan to produce hydrogen on-site using auto-thermal reforming of pipeline supplied natural gas in a Reformer Room but during my study it was directly supplied by gas bottles. The store holds other gases each to a maximum of 50 liters (10 Nm^3);

- 3 × pallets, each palet containing up to 16 H_2 hydrogen bottles
- 3 × pallets, each palet containing up to 16 CH_4 methane bottles
- 1 × pallets, the palet containing up to 16 Ar Argon bottles
- 3 × pallets, each palet containing up to 16 H_2/CO bottles
- 2 × pallets, each palet containing up to 16 N_2/CO bottles (Figure 4.5)

Figure 4.5. Gas bottle storage and distribution room

The FCATS Room provides the Fuel Cell automated Test Station (FCATS) which provides for unattended monitoring and control of test pieces from a single fuel cell to a large fuel cell stack. FCATS is a Windows-based system and responds to safety set-points in combination with other hard-wired automated responses. FCATS provides;

- on-line gas mixture composition control
- real time data logging
- monitoring and control of temperature, pressure and flow rates
- computer monitoring system
- alarm and emergency response triggers
- programmable load control (constant voltage, constant current, constant power, constant resistance)
- PID control of temperature and pressure
- Real-time voltage monitoring

The block diagram Figure 4.6 below illustrates the connections between FCATS, the facility and the fuel cell.

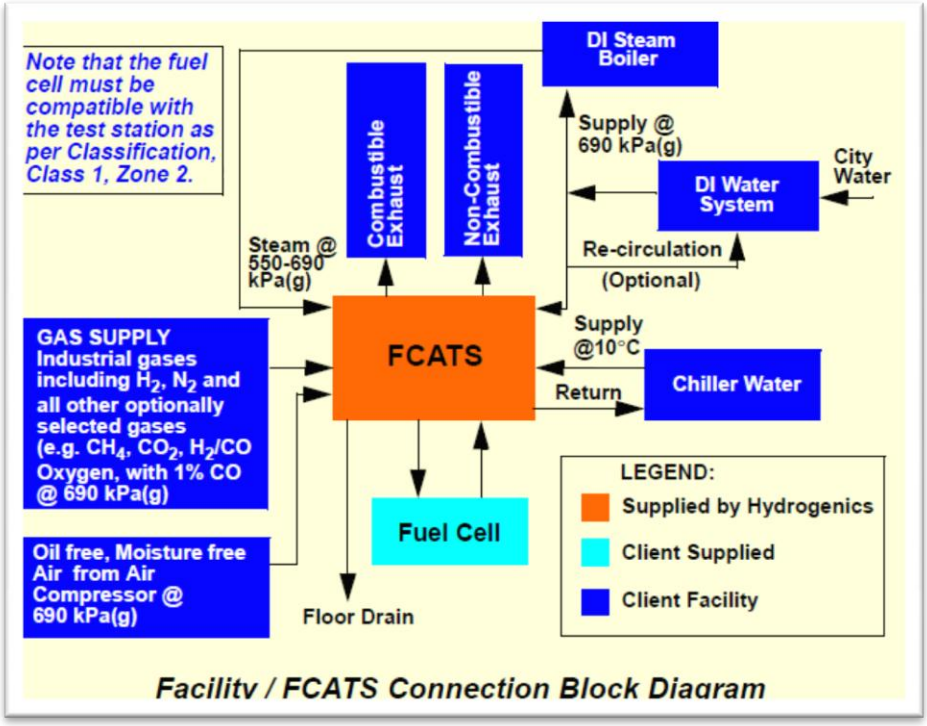

Figure 4.6. Connection between FCATS and other facilities

Gas supply station indicated at Figure 4.6 requires each gas supply at a pressure between 690 to 725 kPa (g) nominal inlet to ensure proper operation of the mass flow controllers (MFCs). All gas supplies are dry. The anode gas supply consists of hydrogen, carbon dioxide, carbon monoxide, carbon monoxide and nitrogen mixture, nitrogen, methane and the cathode gas supply consists of air and nitrogen. At my study, only pure hydrogen for anode gas supply and air for cathode gas supply were fed into the fuel cell stack, without mixing with other gases at anode side.

Two gas exhaust ports are located on the back of the station: one for anode gases and one for cathode gases. The exhausts from the test station are as follows:

- Anode exhaust (combustible) at the top of the test station
- Cathode exhaust (combustible) at the top of the test station
- Anode drain at the back of the test station
- Cathode drain at the back of the test station

Heated hoses are provided for the inlet to the fuel cell. The tubing used to connect the FCATS gas delivery and return ports to the fuel cell are stainless steel to handle higher temperatures and avoid damage from rust or embrittlement.

Both the chilled water inlet and outlet are located at the top of the test station. De-ionised water is used to fill the stack coolant line. Once the water fills the deionised water tank and the lines because the water consumption is small requiring the refilling of the line for water that has evaporated or has been drained. The stack coolant de-ionised water is supplied through sanitary connections which are 316 stainless steel to handle higher temperatures and avoid damage from rust.

A floor drain is provided in the location where the FCATS is operated. The drain is located under the machine, and this is where drain water from the Station dew-point vessels, condenser vessels, and steam trap drains from the machine collected.

The FCATS software is central of the fuel cell test and is used to monitor, control and acquire and log all the test parameters throughout the duration of a test. The process parameters are accessed into Anode and Cathode sections. An operator can determine the total flow rate into the fuel cell, pressure and temperatures of the gases applying pre-set operation. Flow rate or stoichiometry (according to Equation 4.1) and dew point or relative humidity (according to inlet temperature and required relative humidity) values are calculated automatically by process conditions.

De-ionised water treatment facility produces de-ionized water for the clean steam generator and for the humidification of the cathode and anode inlet gaseous mixtures to feed the fuel cell stack. It has the capacity of 440 kg/h deionized water at 10 MΩ and 0.1 μS. It composes of two parts named as Christ Septron and Christ Steritron shown at Figure 4.7.

Water enters a chamber which is filled with an ion exchanger. The electrical potential applied to the electrodes causes charged ions such as sodium and chloride to pass through the ion exchange membrane into a concentrate chamber from which they are discarded. All the treatment steps (filtration, reverse osmosis and electrical demineralisation) as well as agents are integrated in the Christ Septron device (comprising huge circular tank at right side of the below picture).

The protection of the storage tanks from contamination with ozone and ultraviolet light is supplied by Christ Steritron unit. The Steritron provides disinfection of demineralised water and systems where ozone is electrolitically generated from the

demineralised water via an integrated ozone cell (rectangular box situated at the left side of the below picture).

Figure 4.7. De-ionised water treatment unit

Gas Boiler unit produces hot steam (possibly 500 kg/h) from tap water to be used by the Clean Steam Generator (Figure 4.8). A 4000 kg gas fired Hocon FR-series high pressure steam boiler is used. Maximum pressure is 12 bar reaching to maximum temperature 192 °C. The FR series is a 'flame return' reverse fired furnace –flame tube boiler. The flame returns to the front side and the flue gases are led into a tube bank to the rear flue outlet. The boiler is insulated rockwool and an aluminium shell plate. The boiler is provided with a boiler feed water pump (centrifugal) placed on the control side of the boiler.

Figure 4.8. Gas boiler unit

Clean Steam Generator unit produces clean steam for the humidification of the reactants using de-ionised water from de-ionised water treatment plant and hot steam from the gas boiler (Figure 4.9). It is capable of pure steam production up to a maximum of 1500 kg/h at 8 bar primary steam pressure.

Figure 4.9. Clean steam generator unit

Geothermal Cooling System unit provides cooling water for various system components using water from a well, drilled 160 m deep into the ground (Figure 4.10). Additionally a dry cooler /chiller on the roof outside can be used for enhanced cooling. It has the capacity of 44 m^3/h pumping rate coming from mono well outside the building.

Figure 4.10. Geothermal cooling system

4.5. Test Module

Test module chosen for validation is the TM PEFC 5-3 i.e. polarization curve for a PEMFC stack as mentioned before. Although polarization curves are widely used by several organizations as a tool for performance benchmarking, these are not always obtained applying the same boundary conditions to the test object. A typical issue that can occur when comparing polarization curves obtained in different laboratories is described by the flow rate applied to the fuel cell stack. Actually, the mass transport limitations are dominant at high fuel utilization, therefore the inlet flow rate provided to the stack causes the important parameter determining the resulting stack performance. In this test module, the test is performed at constant fuel and air stoichiometry i.e. the inlet flow rate is changed with the current density. However for low current densities, the resulting flow rate would be too low, a minimum flow rate is applied to the stack during the test. The following condition is valid for both the anode and cathode;

$$Q_{v,\lambda} = \frac{M}{zF\rho\varphi} NI\delta \quad \text{for} \quad \frac{M}{zF\rho\varphi} NI\delta > Q_{v,min} \tag{4.1}$$

$$Q_{v,\lambda} = Q_{v,min} \quad \text{for} \quad \frac{M}{zF\rho\varphi} NI\delta \leq Q_{v,min}$$

where $Q_{v,\lambda}$ is the volumetric flow rate (dry basis) of the reactant, δ is the ratio that describes the excess amount of inlet reactants (fuel and air) to required amount, M is the molar mass of dry reactant gas, z is the number of exchanged electrons in the electrochemical reaction (2 for the anode, 4 for the cathode), F Faraday constant, N is the number of cells in the stack, ρ is the density of dry reactant gas under standard conditions, φ is the hydrogen or oxygen content in the dry gas mixture and I is the current. The actual volumetric flow rates of the reactant gases during measuring the test outputs are controlled by δ ratio values unless the volumetric flow rate values are smaller than the minimum flow rates $Q_{v,fuel,min}$ and $Q_{v,ox,min}$. These minimum flow rates correspond to flow rates below 0.3 A/cm^2.

There are two types of test inputs (test conditions) as dynamic and static. The inlet flow rates and the current density are the dynamic inputs listed in the Table 4.3 (European Commission Joint Research Centre Institute for Energy Test Results Report, Test No.1b, 2009).Concerning the measurement uncertainties and the sample rates the values given in the following tables are the values commonly available with most of the instrumentations.

Table 4.3. Variable test inputs during test output measurement

Input	Value/Range	Measurement Uncertainty	Sample Rate
i	0.01-1 A/cm^2	±0.025 A/ cm^2	1 Hz
$Q_{v,fuel}$	Corresponding to the equation 4.1.	± 1% Full Scale (maximum flow)	
$Q_{v,ox}$			

The static inputs are the composition of the inlet as anodic and cathodic gas, stack temperature, stoichiometry, gas inlet temperature, dew point temperature. Since temperature distribution is far from uniform throughout the stack, the stack temperature is recommended as the coolant outlet temperature. The dew point temperature is calculated according to the specified relative humidity and inlet reactant temperature as a few degree less than inlet temperature. The composition of anode side is 100% H_2 as purely use and at the cathode side air is used with approximately 21% oxygen and 79% nitrogen content.

The some static test inputs were changed for each test to observe their affect on actual stack average voltage. At one test series, the fuel and oxidant inlet temperature were varied from 50 to 65 °C by 5 °C increase with constant 95% fuel and oxidant inlet relative humidity (RH) and constant fuel and oxidant stoichiometry as 2 to 3 respectively, and at other test series, with constant 60 °C reactant inlet temperature and with same stoichiometry, RH values were changed from 75% to 95 % as shown in Table 4.4. The changes were done according to the stack manufacturer recommended conditions. The coolant inlet temperature were selected 2.5 °C more than reactant inlet temperature. The primarily test outputs are average stack voltage and power. Secondary test outputs are individual cell voltage, outlet gas temperature, inlet-outlet temperature difference.

Table 4.4. Test conditions

Test #	**Coolant inlet temp.**	**Fuel-oxidant inlet temp. °C**	**Fuel-oxidant inlet RH**	**Fuel-oxidant Stoichiometry**
1	52.5	50	95%	2-3
2	57.5	55	95%	2-3
3	**62.5**	**60**	**95%**	**2-3**
4	67.5	65	95%	2-3
5	62.5	60	85%	2-3
6	62.5	60	75%	2-3

Table 4.5 provides for the ambient conditions such as air temperature, pressure and relative humidity prevailing at the test location at the start and at the end of the test.

Table 4.5. Ambient test conditions at the test location

TEST START		**TEST END**	
T_{amb} (°C)	20	T_{amb} (°C)	24
RH (%)	30	RH (%)	30
P_{amb} (hPa)	991	P_{amb} (hPa)	991

4.6. Test Start-up, Conditioning and Operation Steps

The start-up procedure of the stack consists of heating the stack to the coolant outlet (stack) temperature, using the deionized water coolant with a flow rate 25 lpm. No fuel and oxidant flow occurs during this warm-up of the stack. It is ended up when the coolant temperature reachs to the stack temperature set point, T_{stack}. This is followed by the conditioning of the stack. The humidified reactants are set to their respective inlet temperatures as well as reactant flows. When the temperature set points of both gas streams are attained, their δ ratios are applied with a minimum flow rate corresponding to 300 mA/cm^2 current density. When the flow rates are arranged, the current density is varied from zero (open circuit voltage condition, OCV) to 1000 mA/cm^2 at a rate of 100 mA/cm^2 per minute using the electronic load in the constant current mode. The increase in flow rate corresponding to the increase in current density is operated by the test equipment applied in load following mode. When the maximum current density of 1000 mA / cm^2 is attained, at least 30 minute of stack operation (conditioning) at this current density without changing the test inputs follows. The imposed current density profile for conditioning shown in Figure 4.11 and 4.12 given for 60 ℃ reactant inlet temperature and 95% RH sample (test number 3). The check on attainment of a stability criterion for test inputs and outputs are carried out offline. It is important to operate the stack under stable conditions prior to the start of measurement of test outputs. For conditioning, the coolant inlet temperature (test input) is considered stable when the range of the values measured during 30 minutes is within the measurement uncertainty ($\pm$ 2 $°C$). The stack voltage (test output) is considered stable during this period when the relative standard deviation (RSD) is less than 1%. The range of the measurement

uncertainty (standard deviation) of the stack coolant inlet temperature for the entire 30 min of conditioning is indicated as dotted lines in Figure 4.11.

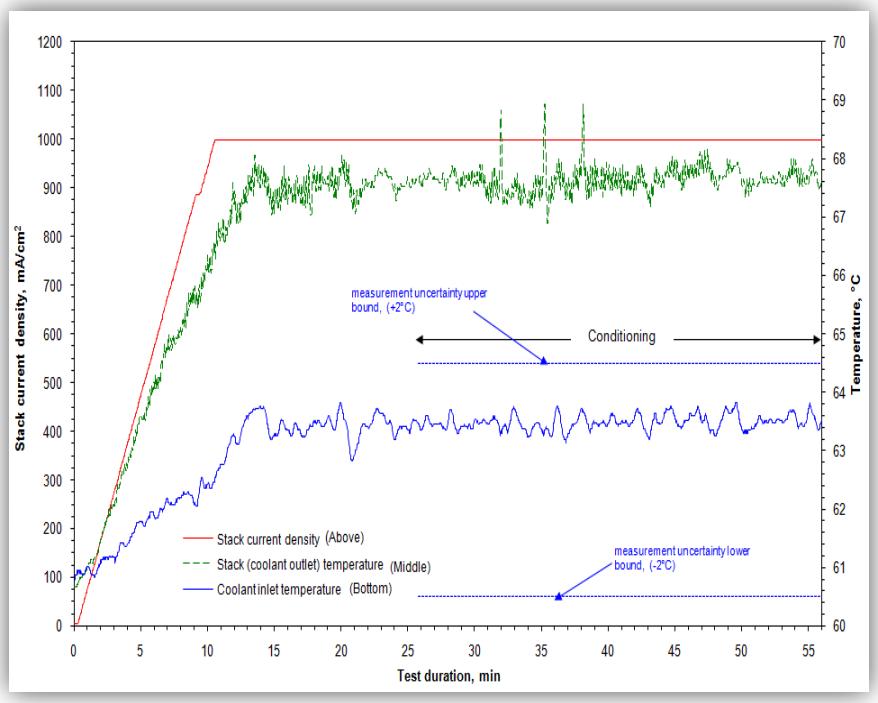

Figure 4.11. Stack coolant inlet and outlet temperature and current density profile during stack conditioning

The upper and lower stability limits corresponding to 1% RSD of the stack voltage averaged over the entire 30 min. conditioning is given in Figure 4.12 by dotted lines. The average stack performance are taken from a total of 1800 acquired data points (1 Hz sampling rate) during conditioning.

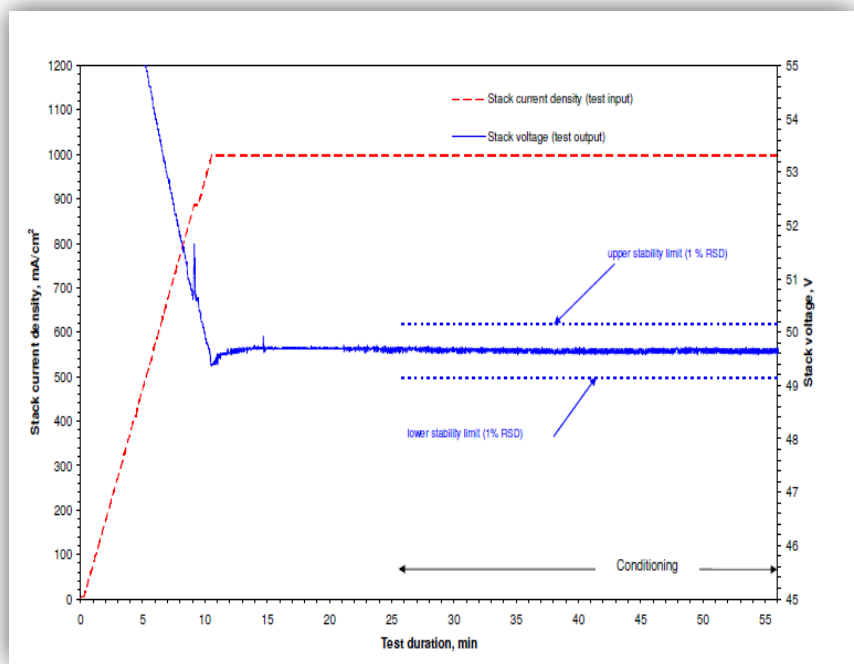

Figure 4.12. Stack current density profile and resulting stack voltage during conditioning

The uncertainties of the measurements expressed as standard deviation are given in Table 4.6 for 60 ℃ reactant inlet temperature and 95% RH (test number 3).

Table 4.6. Average stack performance at conditioning period

Conditioning Duration (min)	**Current Density (mA/cm^2)**	**Average stack Voltage (V)**	**Average stack Power (V)**	**Average stack Temperature (°C)**
30	1000	50.083±0.05	10.017±0.05	63.01±0.20

After 30 min. conditioning phase of the stack at maximum current density 1000 mA/cm^2, the polarization curve is recorded. It consists of imposing a profile onto the stack by drawing current according to the scheme of set points k given in Table 4.7. The scheme comprises in total 15 set points (k=1 to k=15) decreasing current density from the maximum of 1000 mA/cm^2 to 10 mA/cm^2 (set points k=1 to k=8) followed by an increase in current up to the maximum (set points k =9 to k =15).

Table 4.7. Set Points k and corresponding current density values at voltage measurement step

Set points, k	Current density (mA/cm^2)	Set points, k	Current density (mA/cm^2)
1	1000	9	50
2	800	10	100
3	600	11	200
4	400	12	400
5	200	13	600
6	100	14	800
7	50	15	1000
8	10	-	-

The tests were performed two times and Figure 4.13 shows the results giving the each drawn current density step decreasing from 1000 mA/cm^2 to 1 mA/cm^2 and followed by vice versa with respect to the time elapsed completing one current density cycle for the same operation condition as RH 95% and T_{inlet} 60 °C (test number 3).

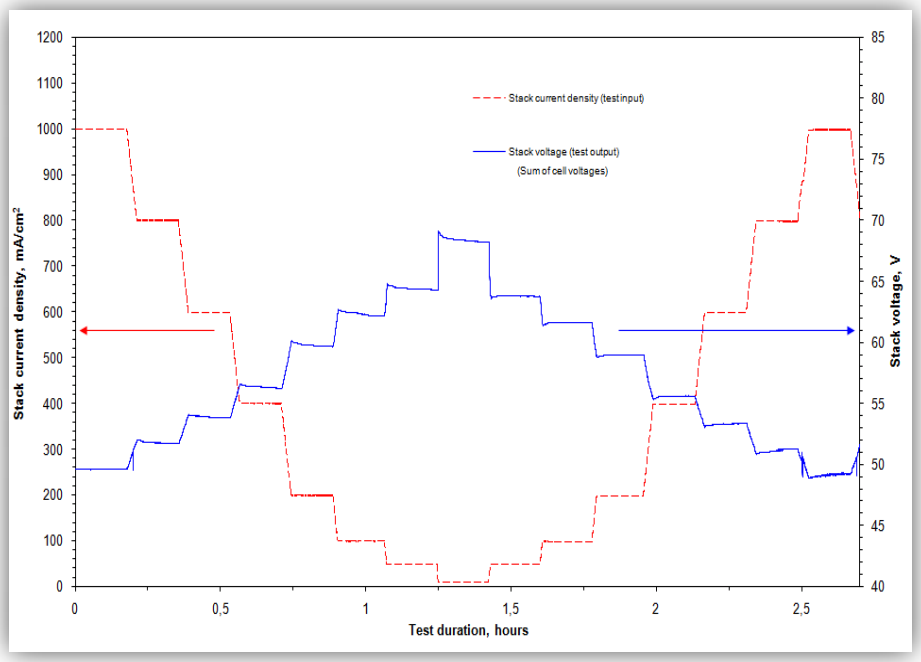

Figure 4.13. Test duration versus stack voltage and stack current density

The current density is changed step by step as shown above and the duration time of each step is called t_{int} (dwell time). For each increment of the current density, the reactant flows are adjusted by imposing a new set point for the flows prior to drawing the corresponding current (load following mode). Figure 4.14 and Appendix B illustrates the data acquisition timeline at each current density set point.

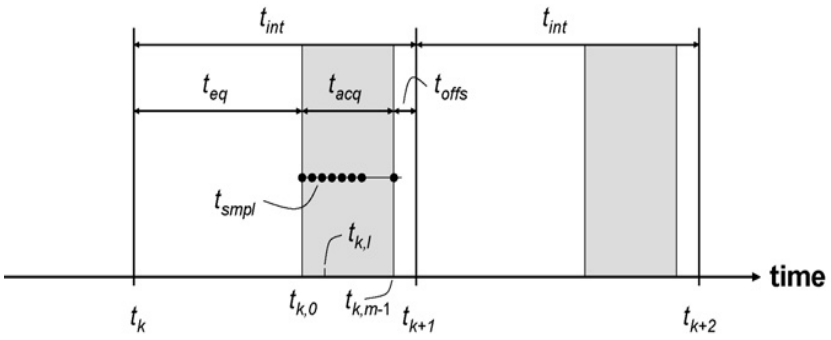

Figure 4.14. Timeline for the data acquisition

Principally, the test module divides the total dwell time at each set point k into three different periods namely, the equilibration period t_{eq}, the period for data acquisition t_{acq} and offset time t_{offs} as shown Figure 4.14. The Figure 4.15 shows the resulting polarization curve for same operation condition sample. The stack voltage value reported at each set point of the polarization curve is the mean value of those recorded during the acquisition timeline.

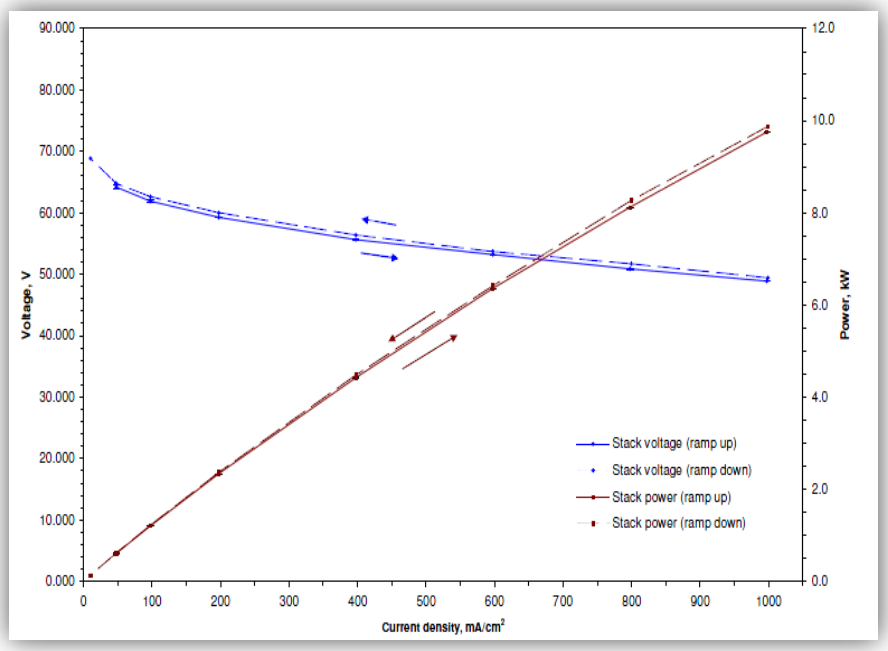

Figure 4.15. Polarization curve of the stack

The average stack voltage versus current density graph (polarization curve) and power versus current density graph are slightly higher when the current density is decreasing from set point k =1 (1000 mA/cm^2) to set point k =8 (10 mA/cm^2) compared to the increasing case from set point k =8 to set point k =15 (Figure 4.15) without overlapping with each other despite the same process conditions and methods are applied. Probably this is due to the stack produced more water at higher current density than at lower values which are providing better hydration of the electrolyte membranes of the stack. This would supply an increased proton conductivity and swelling of the membrane thereby reduces the internal stack resistance and minimises voltage losses.

Briefly, at Institute for Energy (IE) PEM fuel cell stack performance testing facility, before starting to polarization curve test, the stack is always conditioned by heating the stack to the test temperature by using the coolant. Both anode and cathode sides are purged with N_2 for 5 minutes. The reactant gases are then turn on and the current is ramped up to 1000 mA/cm^2 in ten minutes and held there for 30 or 40 minutes before starting the test. As part of the test validation the FCTEST procedure, it should be checked if in the last 30 minute of the test conditioning step, the stability criteria were met. Then the test output measurement starts by drawing current from the stack and polarization curve can be obtained from the average voltage values for each step

point versus corresponding current (density) value for decreasing current from step 1 to step 8 or increasing current from step 8 to step 15 in order to assess the stack power performance that is easily calculated as voltage multiplied by current. After the completion of the test, the stack is purged with N_2 for 20 to 30 minutes.

CHAPTER 5

RESULTS AND DISCUSSION

Experimental study comprise of the effects of different temperatures and relative humidities onto 10 kW peak power stack performance and the experimental data were fitted into early developed semi-empirical nonlinear model to find the model parameters. Their variations with temperature and relative humidity (RH) are observed via parameters versus temperature and RH graphs. The fitting was done by LABfit Curve Fitting Software that is specialized on nonlinear regression. LABfit was easily made the data fitting into model showing the goodness of fit and residuals values. For model selection, The Fuel Cell Handbook model was taken as a reference with its model simplicity with less number of parameters than Kim's model and more mechanistic background than both Kim's and Amphlett' s models.

When the current density is obtained from the stack, there are some voltage losses that badly affect the stack performance that is well profiled at Figure 2.3 as called polarization i-V curve. These losses are explained as kinetic loss that dominates at low current density related to the initiation of the electrochemical reaction at both anode and cathode sides and ohmic loss that is mainly observed at the average current densities due to mostly membrane resistance to proton flows and the mass transfer loss occurs dominating at higher current densities. Due to Instiute for Energy (IE) fuel cell stack testing facility (FCATS) is attained to maximum 1000 mA/cm^2 current density, the mass transfer loss effect was not observed at my study that can be clearly seen by making comparison between Figure 2.3 and Figure 4.15. Therefore the mass transfer loss term in the model was neglected and thus the limiting current density (i_L) parameter was omitted from the parameter estimation of data fitting. In this case, the parameters included in the model are reduced to three as charge transfer coefficient (α), exchange current density (i_o) for cathode side and ohmic resistance (R_{int}).

At IE test system, for each current density steps, variation on coolant outlet temperature occurs due to heat generation inside stack during operation at high current densities. Between the highest current density and lowest current density values, approximately 6 ℃ coolant outlet temperature difference generates. Due to this

variation on coolant outlet temperature and the lack of the temperature sensors inside the stack, it is deemed that the stack temperature is equal to coolant outlet temperature. The values of the coolant oulet temperatures of each current density step were averaged for a polarization curve from k=1 to k=8 to form the average stack temperature. The thermodynamic reversible voltage was calculated according to equations from 2.5 to 2.13 in section 2.2.1 and put inside the model as a constant average value based on the assumption of constant average stack temperature.

The effects of varying inlet reactant temperatures to fuel cell stack were experimented according the test protocol presented at Chapter 4. The results shown in the Figure 5.1 were obtained for the descending direction of current density. The inlet temperature was changed from 50 °C to 65 °C with 2/3 fuel to oxidant stoichiometry and 95% relative humidity. From the graph it is clearly seen that at higher current densities (800 and 1000 mA/cm^2) the temperature increase improves the stack performance. At maximum current density, the measured voltage at 65 °C is 2 V higher than the voltage measured at 50 °C. As conclusion, at higher current densities the stack performance is improved by higher temperature values.

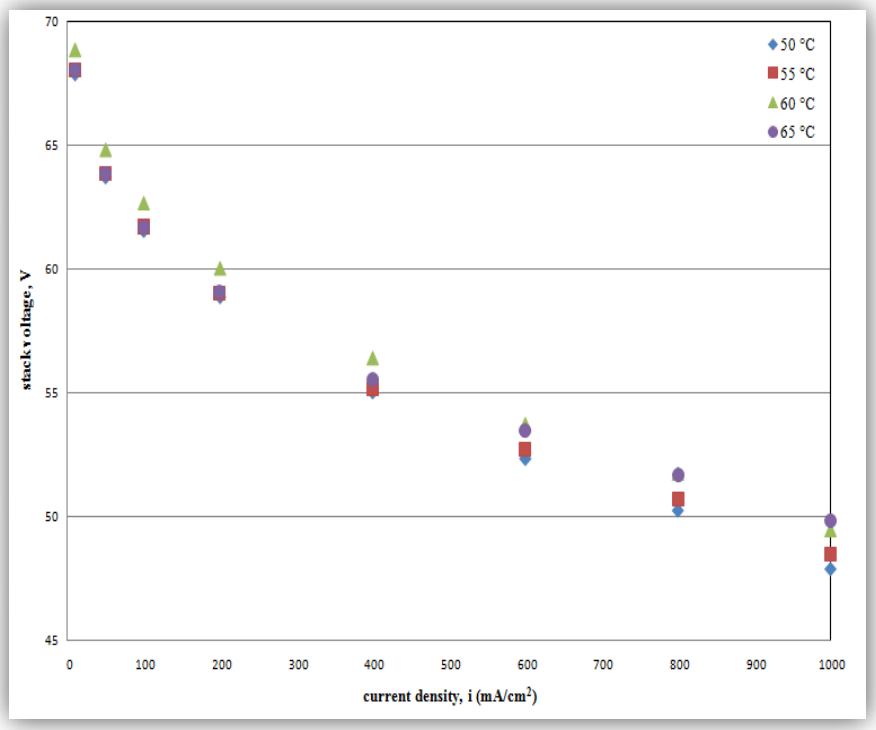

Figure 5.1. Descending direction polarization curve for different temperatures

Similar research can be found in the literature studying the temperature effect on the stack behavior because temperature is a critical issue for fuel cell operation system. One was studied temperature effect from 65 to 85 °C with 1.2 to 2 for fuel to air stoichiometry and fully humidification of reactants (100%) having larger temperature range but applying to much smaller stack than IE FCstack (Yan et al., 2006). In that case, the increase was observed from 65 to 75 °C but while reaching to 85 °C, there is a degradation on voltage. This shows how important to provide temperature balance for fuel cells. For the first case, gas diffusivity and ohmic ionic conductivity of Nafion membrane are improving with increasing the temperature but for the second case with further increase of temperature, membrane humidification problem appears due to the reduction of the reactant gases relative humidities and water content inside the membrane blocking the proton flow. If the temperature reachs to the critical temperature where the amount of evaporated water exceeds the amount of produced water from stack, the membrane will start to dry out. This would cause to ohmic resistance increase and eventually the stack is highly damaged.

The varying reactant humidification from 75% to 95% relative humidity (RH) does not make explicitly difference on the stack voltage as shown in Figure 5.2 due to the limited RH range. While testing made for the condition of 75 % RH, roughly terminal ten cells of the stack deteriorated and decreased to under the minimum cell voltage value (0.2 V) means that alarm case was happened and the system automatically shut down itself. Because of the sensitivity of the stack to low reactant humidification, that could not be possible to try an effect of much lower relative humidities than 75%. Humidification is one of the significant facts of fuel cells for proton pass inside the membrane. Normally if the membrane is enough humid, hydrophilic side of the membrane sulfonic acid groups can facilitate the proton passage through the membrane but if not, proton pass stops and membrane can dry out soon. It is expected that higher the relativity humidity provides higher the performance achievement however too much humidity can block the gas diffusion porosity by flooding. This may be the reason of 85% RH condition shows better performance than 95% case. However this is only an uncertain interpretation because of the slight differences between RH values.

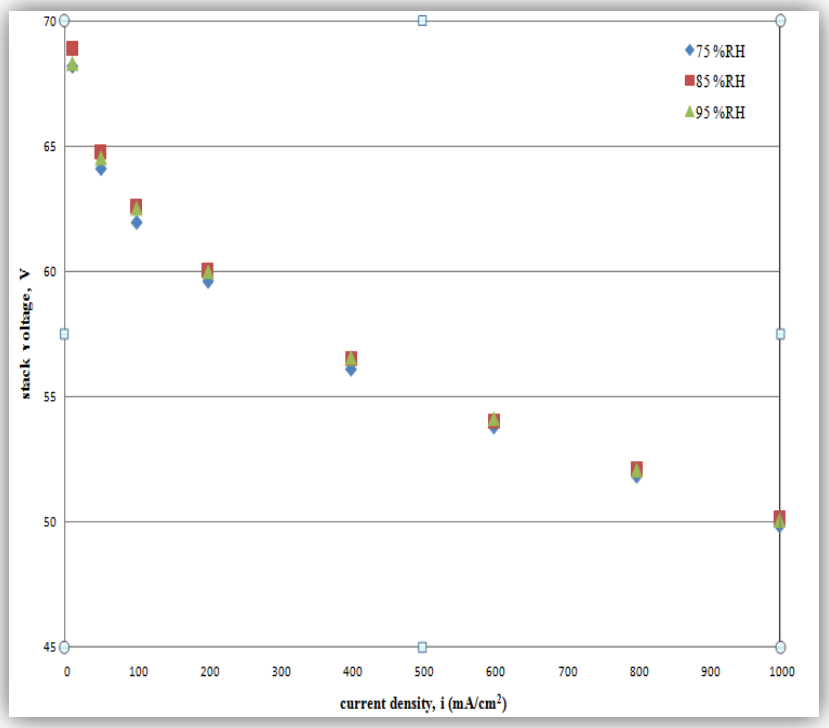

Figure 5.2. Descending direction polarization curve for different relative humidities

In literature, the effects of anode and cathode reactant humidification on cell and stack performance were tested seperately with each other by keeping constant anode side by merely varying cathode humidification or vice versa. The reactant humidification range were not restricted due to small scale stack used (with 49 cm^2 active area and 9 cells) and they could make tests much lower RH values than IE test range for relative humidity i.e. one study was down to 10% RH for cathode and 70% RH for anode. The best case performance was achieved for low air humidity levels occured when the highest hydrogen humidity level was carried out. This observation was consistent with the results of Nguyen and White (1993) who found at high current density the transport from the anode by elecro-osmotic drag exceeds transport to the anode by back diffusion from the cathode thus leading to the membrane dehydration at anode side while cathode catalyst layer of membrane has more humidity due to higher water generation rate and electro-osmotic drag. At low current density, when the anode is dry, the produced water at the cathode side pass through membrane by back diffusion and this results of the water deficiency in the cathode catalyst layer. Therefore humidification of anode catalyst layer plays an important role for the sufficient hydration of the membrane and enhances the operation. On the other hand, the change

on the cathode humidification did not affect considerable on fuel cell or stack performance (Amirinejad et al., 2006).

It is often applied way to represent emprical data using a model based on mathematical equations. With the correct model, one can determine important characteristics of the data i.e. in this study, the reaction kinetics on both side, membrane proton conductivity, reactants mass transfer trend from the gas diffison layer to catalyst layer. The aim of the data fitting is to find the parameter values that most closely match the data. The models to which data are fitted depend on adjustable parameters. To perform fitting, the function that measures the closeness between the data and the model is defined (Equation 3.7). This function is minimized to the possible smallest value with respect to the model parameters. For linear models, the function differentiation with respect to parameters and setting the derivatives equal to zero can solve parameters that minimize the function. However in nonlinear models, it is not feasible to solve the function for the parameters due to the complexity of function therefore various iterative procedures are used starting with initial guess of parameter values.

The widely used iterative procedure for nonlinear curve fitting is the Levenberg-Marquardt algorithm (LMA) which good fitting softwares implement. For this study, LABFIT Curve Fitting Software (Nonlinear Regression Program) also uses LMA for data fitting into model. For data fitting only descending direction of current density from 1000 mA/cm^2 to 10 mA/cm^2 could be investigated. From Figure 5.3 to 5.14 the graphs show fitting results of LABFIT and parity plots of experimental stack voltage versus model stack voltage for each test series according to Table 4.4 respectively. The following nonlinear model is used for data fitting simplified from the original model with some omissions;

$$E = \Delta E_{reversible} - \frac{RT}{\alpha zF} In\left(\frac{i}{i_0}\right) - iR_{int} \quad (5.1)$$

The activation loss is only calculated for cathode electrode due to much higher reaction rate of anode side hydrogen oxidation than cathode side oxygen reduction. Anode electrode has more than 1000 times higher exchange current density values (i_o) than cathode exchange current density values. For ohmic resistance case, due to the electron flow resistance value through the gas diffusion layer is less than the ionic resistance inside the membrane thus the primary resistance was neglected.

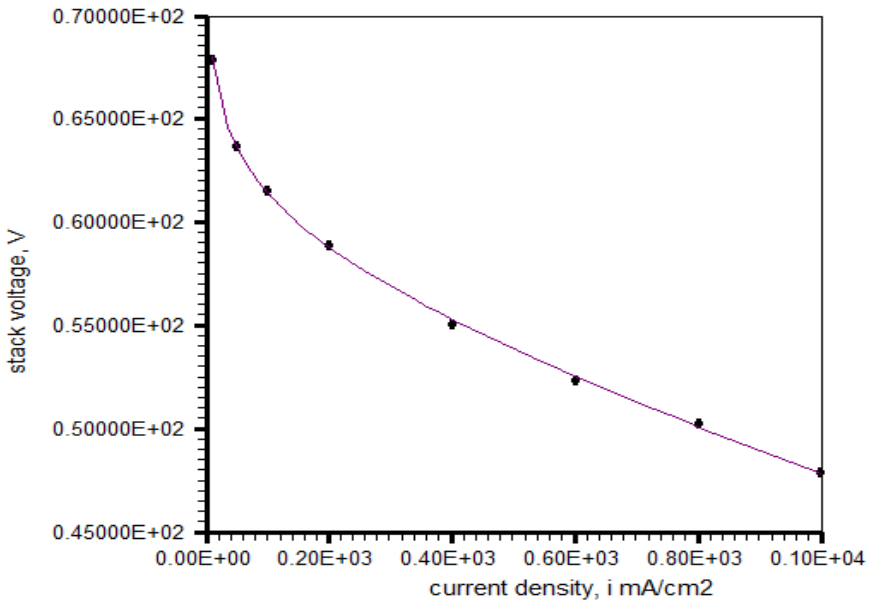

Figure 5.3. Data fitting for test conditions 50 °C temperature, 95% relative humidity (RH) and 2/3 hydrogen to air stoichiometry

The parity plot shows the proximity of the experimental and model stack voltage values using y = x linear line.

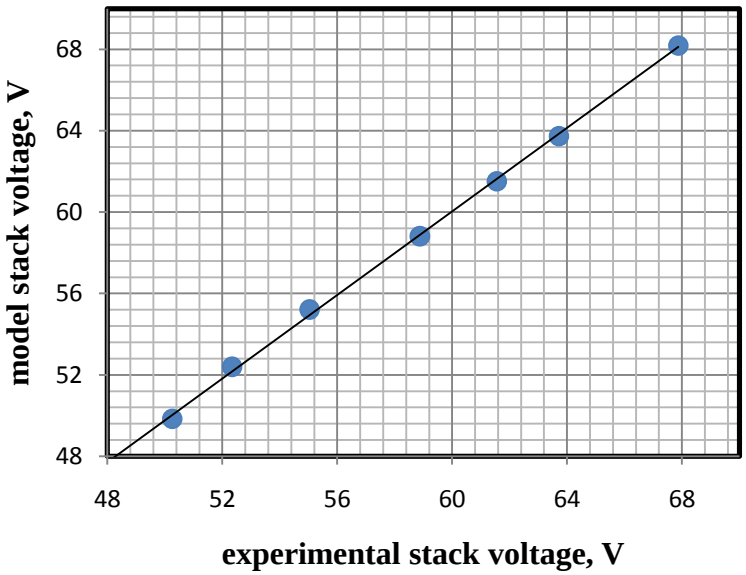

Figure 5.4. The experimental versus model stack voltage for 50 °C temperature, 95% RH and 2/3 hydrogen to air stoichiometry

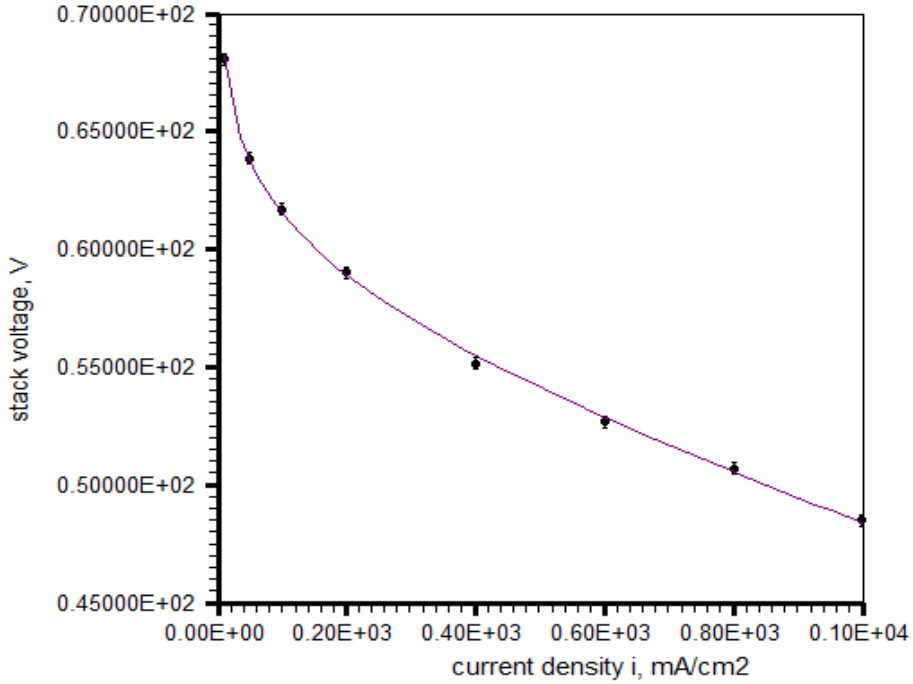

Figure 5.5. Data fitting for test conditions 55 °C temperature, 95% relative humidity (RH) and 2/3 hydrogen to air stoichiometry

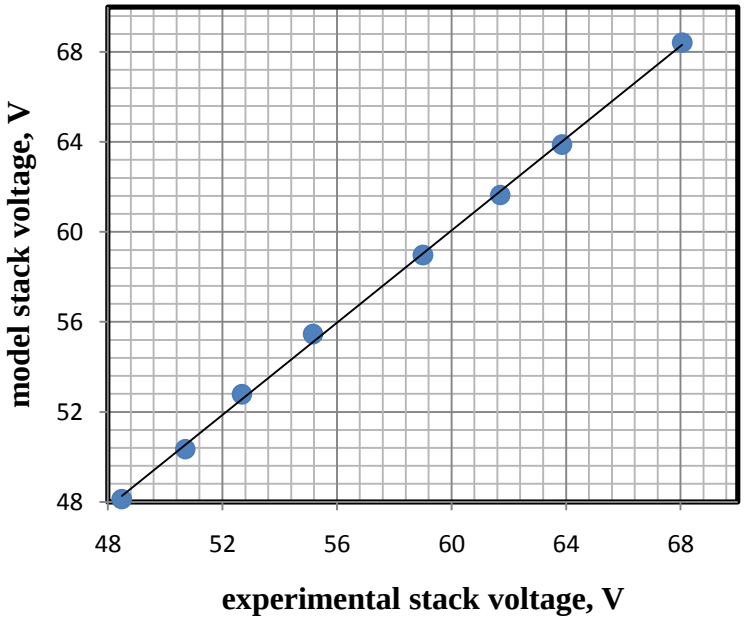

Figure 5.6. The experimental versus model stack voltage for test conditions 55 °C temperature, 95% RH and 2/3 hydrogen to air stoichiometry

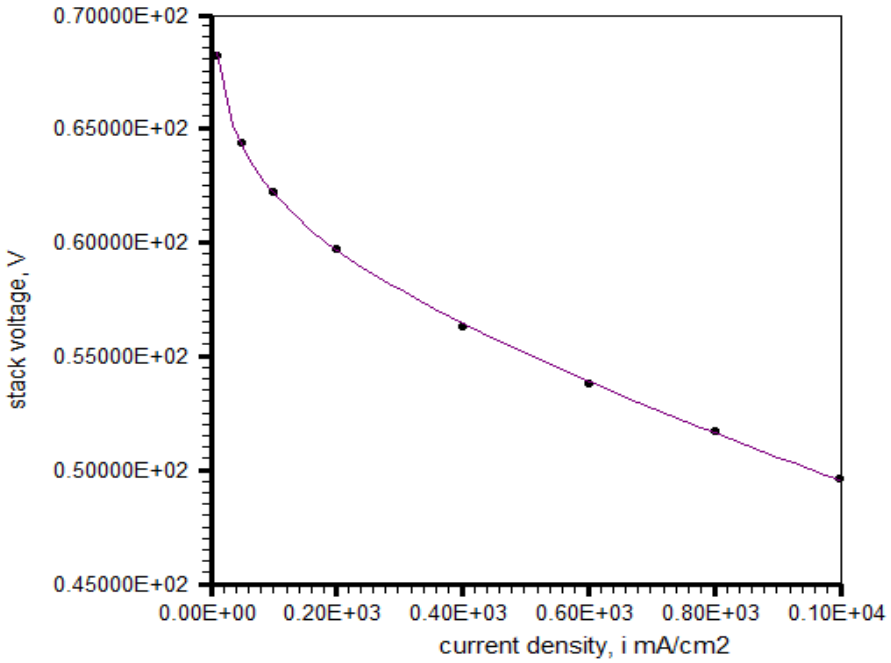

Figure 5.7. Data fitting for test conditions 60 °C temperature, 95% relative humidity (RH) and 2/3 hydrogen to air stoichiometry

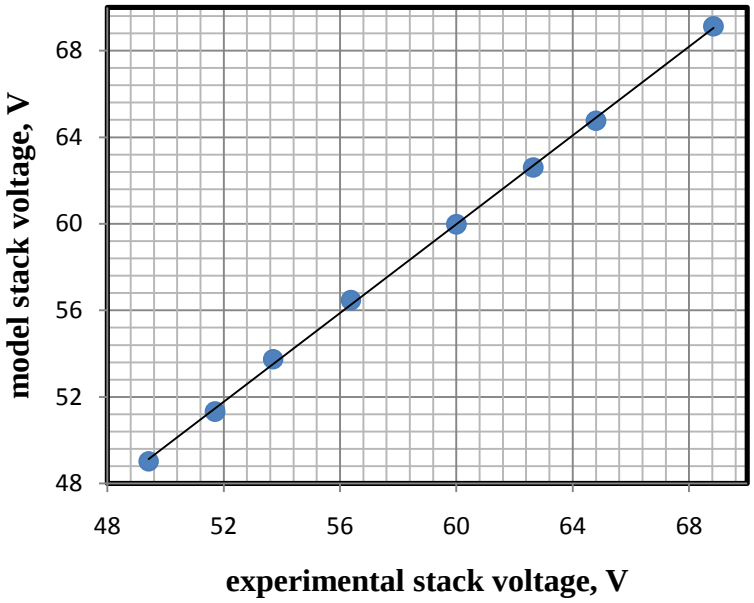

Figure 5.8. The experimental versus model stack voltage for 60 °C temperature, 95% RH and 2/3 hydrogen to air stoichiometry

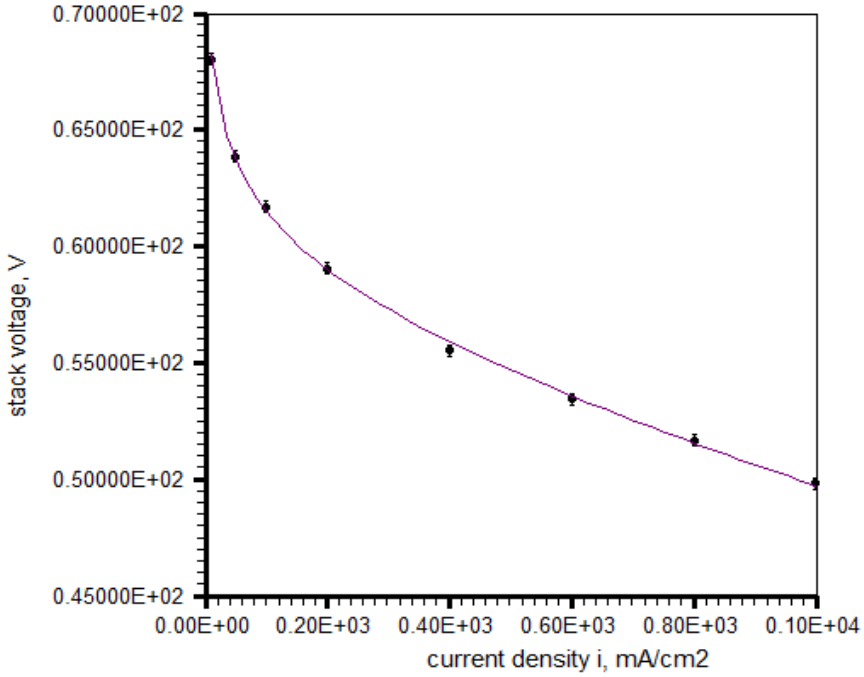

Figure 5.9. Data fitting for test conditions 65 °C temperature, 95% relative humidity (RH) and 2/3 hydrogen to air stoichiometry

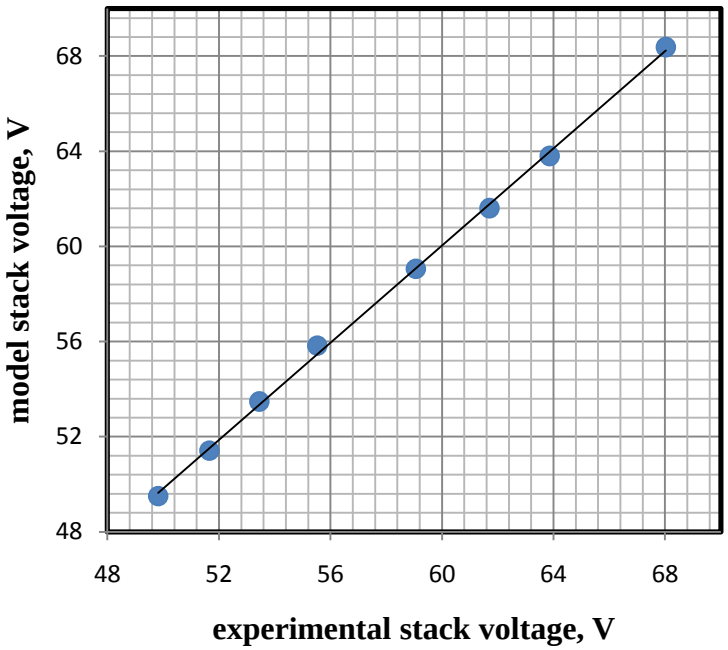

Figure 5.10. The experimental versus model stack voltage for 65 °C temperature, 95% RH and 2/3 hydrogen to air stoichiometry

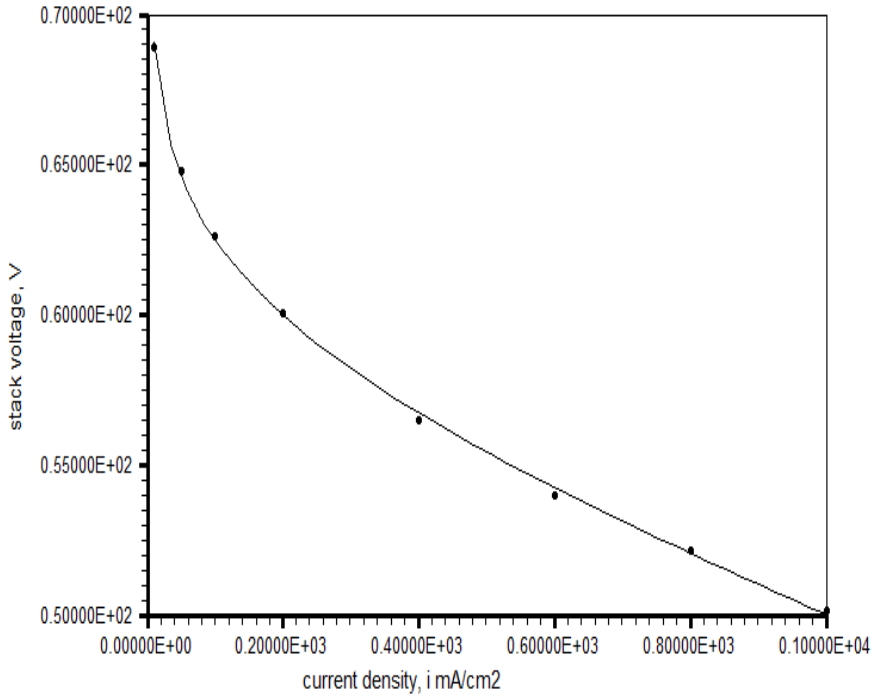

Figure 5.11. Data fitting for test conditions 60 °C temperature, 85% relative humidity (RH) and 2/3 hydrogen to air stoichiometry

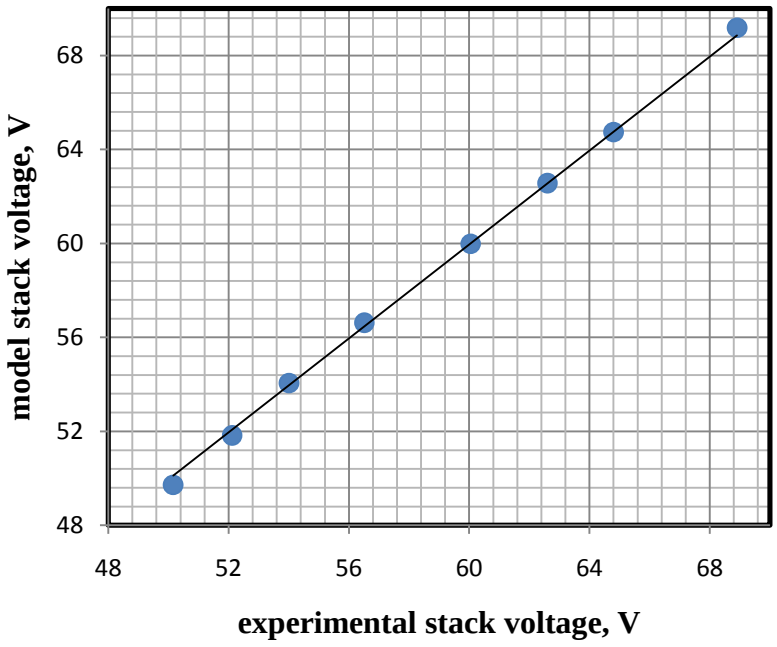

Figure 5.12. The experimental versus model stack voltage for 60 °C temperature, 85% RH and 2/3 hydrogen to air stoichiometry

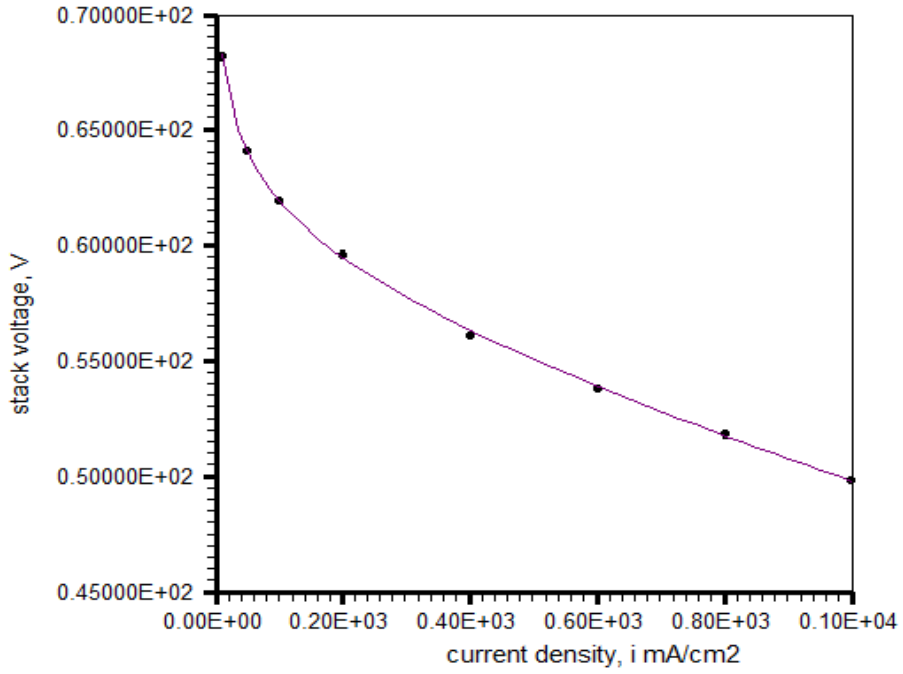

Figure 5.13. Data fitting for test conditions 60 °C temperature, 75% relative humidity (RH) and 2/3 hydrogen to air stoichiometry

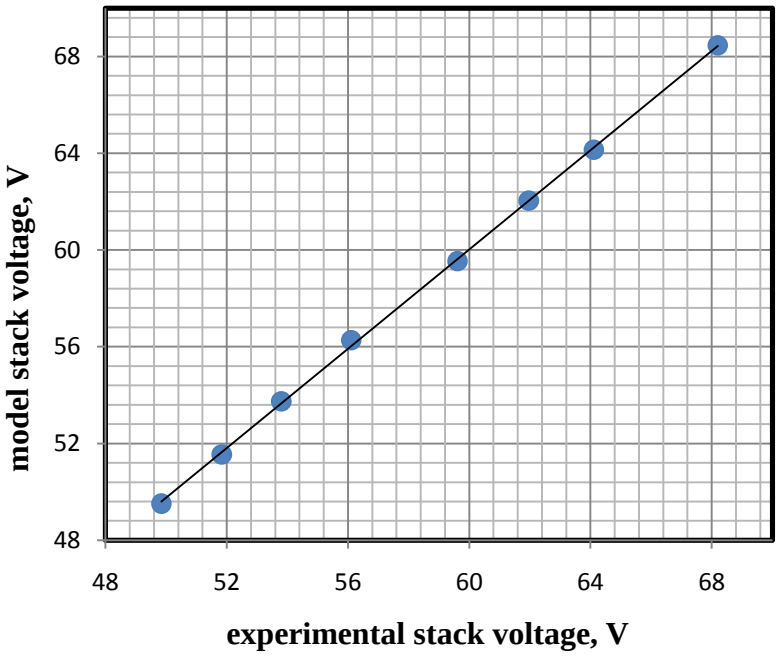

Figure 5.14. The experimental versus model stack voltage for 60 °C temperature, 75% RH and 2/3 hydrogen to air stoichiometry

The experimental data as shown above are well fitted to the nonlinear model. However to determine the accuracy of the fitting, the model parameter values have to be analysed comparing with literature values.

Tables from 5.1 to 5.6 indicate the values of calculated thermodynamic equilibrium potential, experimental stack voltage, model stack voltage including activation and ohmic losses for each current densities for each test conditions in turn according to Table 4.4. Figures from 5.15 to 5.20 show the model voltage and activation and ohmic losses in the same graph according to current density in order to express the losses behaviour.

Table 5.1. Experimental stack voltage, model stack voltage and model voltage losses at each current density step for 50 °C and 95% RH

i (mA/cm^2)	$E_{experimental}$	E_{model} (V)	E_{rev} (V)	$V_{activation}$	V_{ohmic}
1000	47,8863	47,4673	89,0757	32,9909	8,6175
800	50,2534	49,8388	89,1577	32,4248	6,894
600	52,3429	52,3978	89,2635	31,6951	5,1705
400	55,0344	55,2098	89,3234	30,6666	3,447
200	58,8769	58,8140	89,4459	28,9083	1,7235
100	61,5547	61,5076	89,5195	27,1501	0,8617
50	63,7165	63,7310	89,5538	25,3919	0,43087
10	67,8771	68,1797	89,5753	21,3093	0,08617

The results for model stack voltage and activation and ohmic losses are plotted versus current density. From the plot logarithmic behavior of activation loss increases greatly at low current density but then the increase rate gradually slows down at higher current densities. For ohmic loss case, the linear increase behavior is obtained exactly from low to medium scale current densities compatible with its definition.

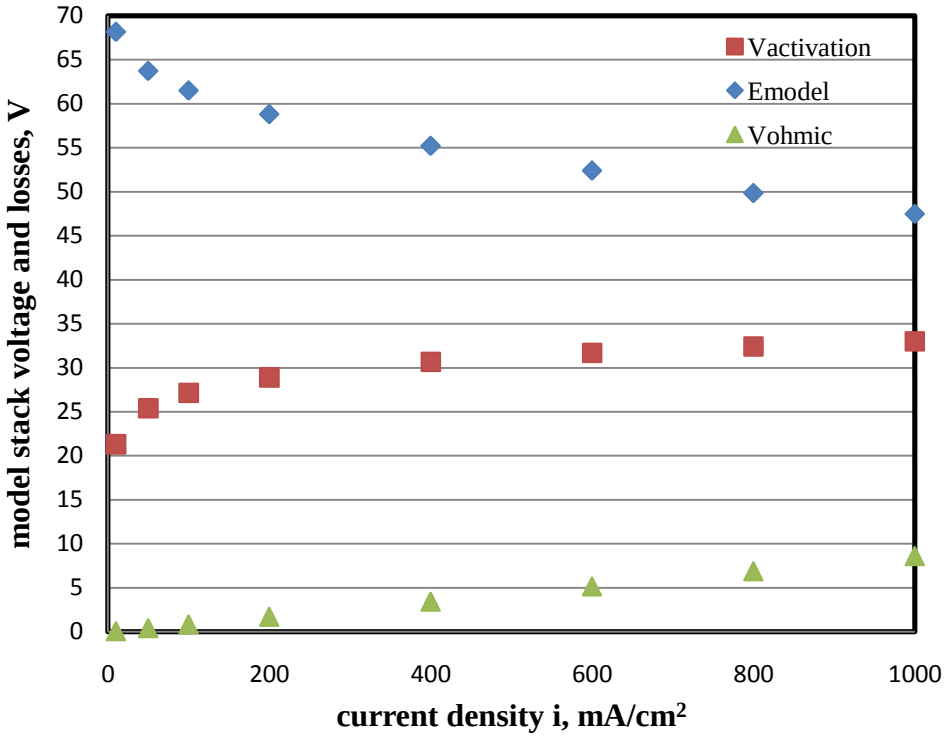

Figure 5.15. Stack model voltage and voltage losses versus current density for 50 °C and 95% RH

Table 5.2. Experimental stack voltage, model stack voltage and model voltage losses at each current density step for 55 °C and 95% RH

i (mA/cm^2)	$E_{experimental}$	E_{model} (V)	E_{rev} (V)	$V_{activation}$	V_{ohmic}
1000	48,485	48,1219	88,6565	32,6370	7,8975
800	50,700	50,3478	88,7212	32,0553	6,318
600	52,683	52,7836	88,8276	31,3054	4,7385
400	55,166	55,4602	88,8678	30,2486	3,159
200	59,004	58,9725	88,9938	28,4418	1,5795
100	61,703	61,6431	89,0679	26,6350	0,7897
50	63,862	63,8813	89,1044	24,8282	0,3948
10	68,057	68,4142	89,1263	20,6330	0,0789

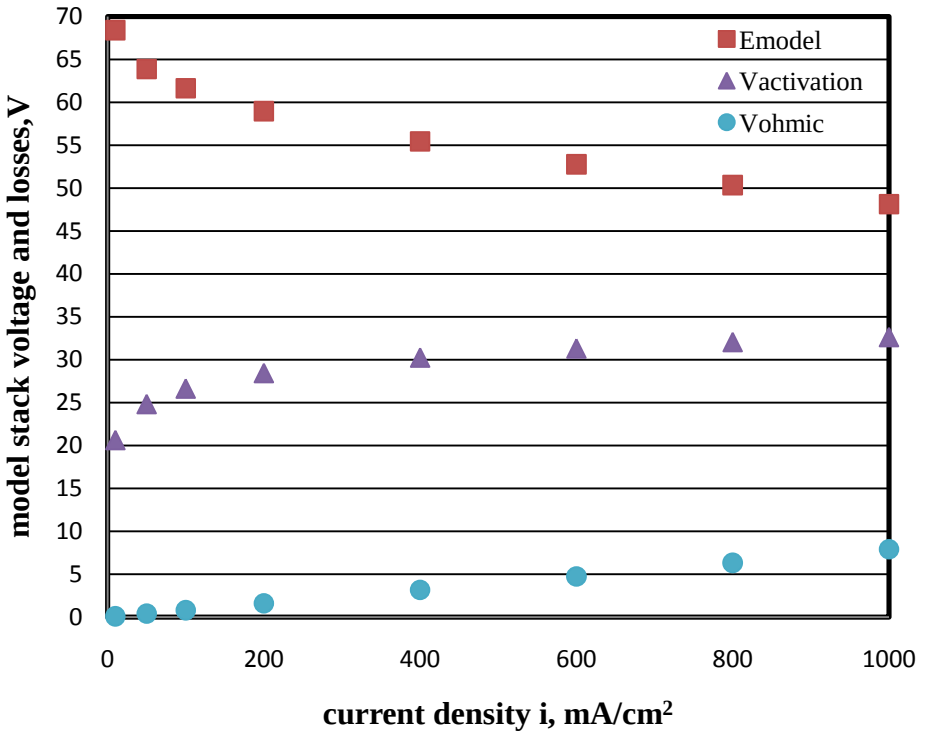

Figure 5.16. Stack model voltage and voltage losses versus current density for 55 °C and 95% RH

Table 5.3. Experimental stack voltage, model stack voltage and model voltage losses at each current density step for 60°C and 95% RH

$i(mA/cm^2)$	$E_{experimental}$	E_{model} (V)	E_{rev} (V)	$V_{activation}$	V_{ohmic}
1000	49,415	49,0284	88,3720	31,0823	8,2612
800	51,703	51,3246	88,4605	30,5268	6,609
600	53,700	53,7475	88,5150	29,8107	4,9567
400	56,374	56,4722	88,5780	28,8013	3,3045
200	60,001	59,9783	88,7063	27,0757	1,6522
100	62,641	62,6002	88,7766	25,3502	0,8261
50	64,800	64,7639	88,8017	23,6247	0,4130
10	68,839	69,1245	88,8253	19,6181	0,0826

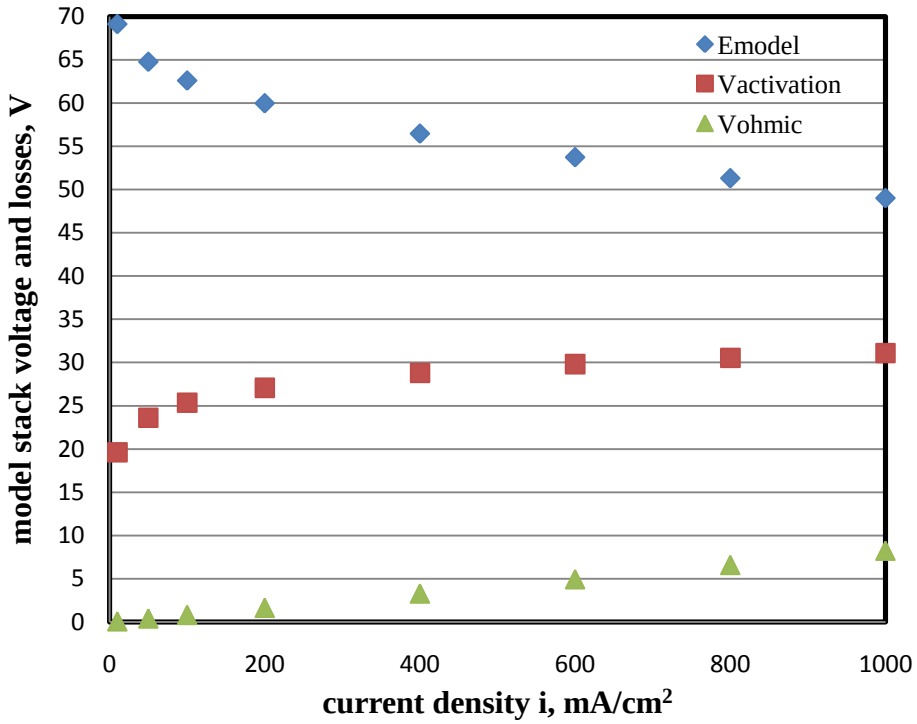

Figure 5.17. Stack model voltage and model losses versus current density for 60 °C and 95% RH

Table 5.4. Experimental stack voltage, model stack voltage and model voltage losses at each current density step for 65°C and 95% RH

$i(mA/cm^2)$	$E_{experimental}$	$E_{model}(V)$	$E_{rev}(V)$	$V_{activation}$	V_{ohmic}
1000	49,819	49,5019	88,0718	32,3313	6,2385
800	51,657	51,4116	88,1368	31,7344	4,9908
600	53,449	53,4793	88,1872	30,9647	3,7431
400	55,523	55,8290	88,2044	29,8800	2,4954
200	59,065	59,0551	88,3284	28,0256	1,2477
100	61,700	61,6078	88,4029	26,1712	0,6238
50	63,861	63,8013	88,4301	24,3168	0,3119
10	68,032	68,3744	88,4479	20,0111	0,0623

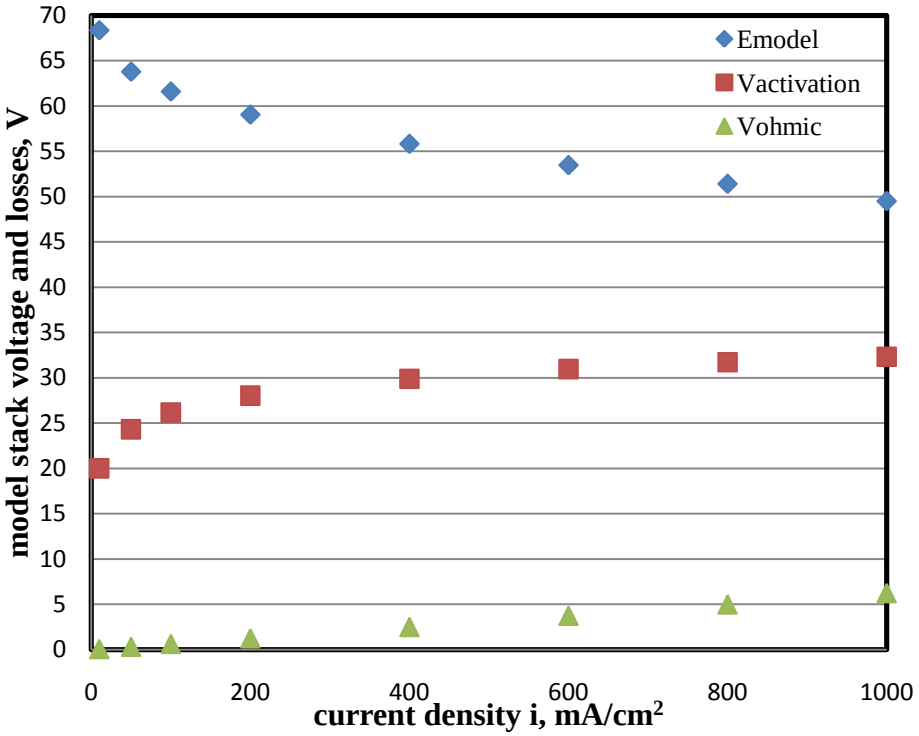

Figure 5.18. Stack model voltage and voltage losses versus current density for 65 °C and 95% RH

Table 5.5. Experimental stack voltage, model stack voltage and model voltage losses at each current density step for 60°C and 85% RH

$i(mA/cm^2)$	$E_{experimental}$	$E_{model}(V)$	$E_{rev}(V)$	$V_{activation}$	V_{ohmic}
1000	50,156	49,7199	88,3749	31,4040	7,251
800	52,118	51,8266	88,4561	30,8287	5,8008
600	54,009	54,0588	88,4965	30,0870	4,3506
400	56,514	56,6233	88,5653	29,0416	2,9004
200	60,046	59,9840	88,6887	27,2545	1,4502
100	62,606	62,5670	88,7595	25,4674	0,7251
50	64,800	64,7435	88,7864	23,6803	0,3625
10	68,909	69,1830	88,7864	19,5308	0,0725

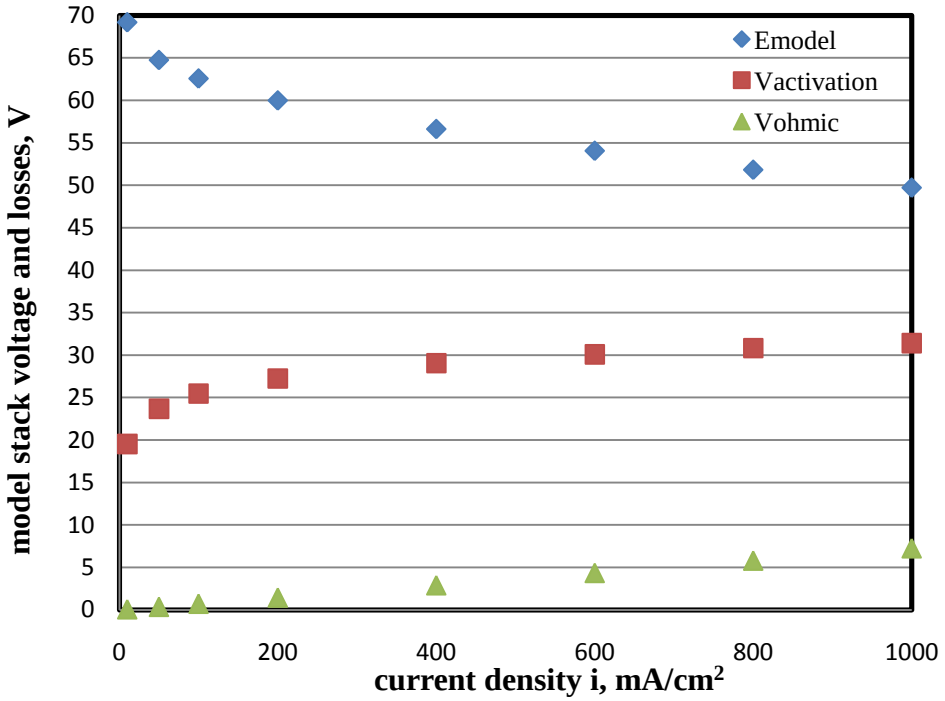

Figure 5.19. Stack model voltage and voltage losses versus current density for 60 °C and 85% RH

Table 5.6. Experimental stack voltage, model stack voltage and model voltage losses at each current density step for 60°C and 75% RH

$i(mA/cm^2)$	$E_{experimental}$	$E_{model}(V)$	$E_{rev}(V)$	$V_{activation}$	V_{ohmic}
1000	49,8459	49,5138	88,3455	31,7096	7,122
800	51,8336	51,5449	88,3962	31,1536	5,6976
600	53,7992	53,7445	88,4545	30,4367	4,2732
400	56,1059	56,2697	88,5450	29,4264	2,8488
200	59,6137	59,5349	88,6587	27,6993	1,4244
100	61,9631	62,0407	88,7251	25,9722	0,7122
50	64,1143	64,1480	88,7492	24,2450	0,3561
10	68,1981	68,4548	88,7608	20,2347	0,0712

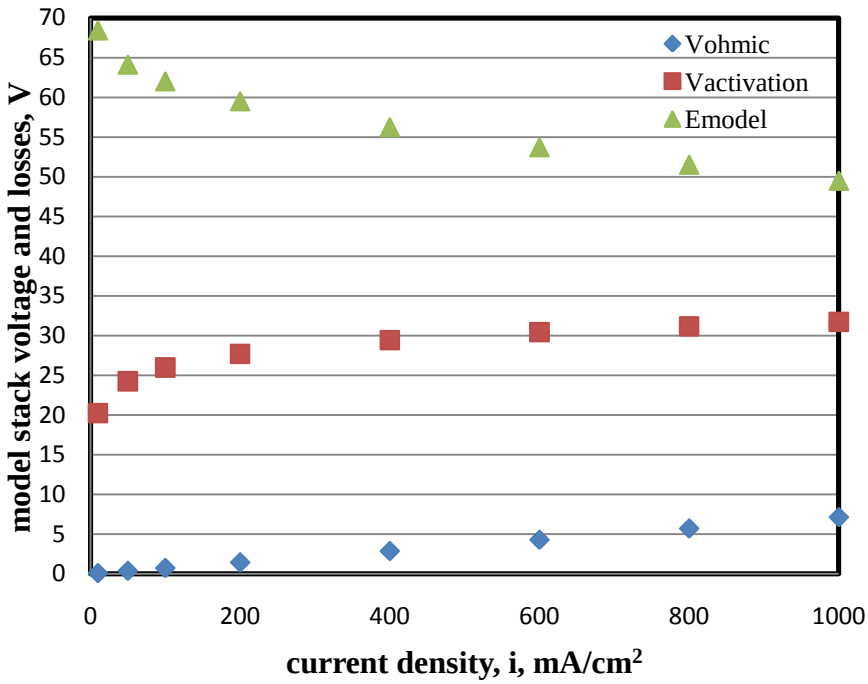

Figure 5.20. Stack model voltage and voltage losses versus current density for 60 °C and 75% RH

From Tables 5.1 to 5.4 the thermodynamic reversible Nernst voltage slightly decreases with temperature increase. This opposite correlation is coherent with the Nernst voltage variation characteristic with temperature change relating to Nernst equation and at typical fuel cell operating temperatures (for PEM fuel cells) of 60-80 °C, the theoretical cell voltage is 1.2-1.18 V. The tested fuel cell stack has 75 cells so when the theoretical stack voltage is divided into the cell number, the value is approximately near to this given cell voltage range.

The temperature variation for model stack voltage values was shown from table 5.1 to 5.4 and this values increase slightly with temperature from 50 °C up to 65 °C. The same temperature variation effect was also attained for the experimental stack voltages for especially higher current densities (Figure 5.1). However, the model stack voltage for 60 °C obtained slightly higher value than the stack voltage for 65 °C. Unfortunately, this opposite behaviour was observed at the activation and ohmic loss terms. Normally the activation loss should decrease with increasing temperature up to 65 °C due to the reaction kinetic acceleration. However the contrast was again obtained from 60 °C to 65 °C with slight activation loss increase. Figure 5.21 shows the activation loss at 65 °C higher than 60 °C that does not have any reasonable explanation.

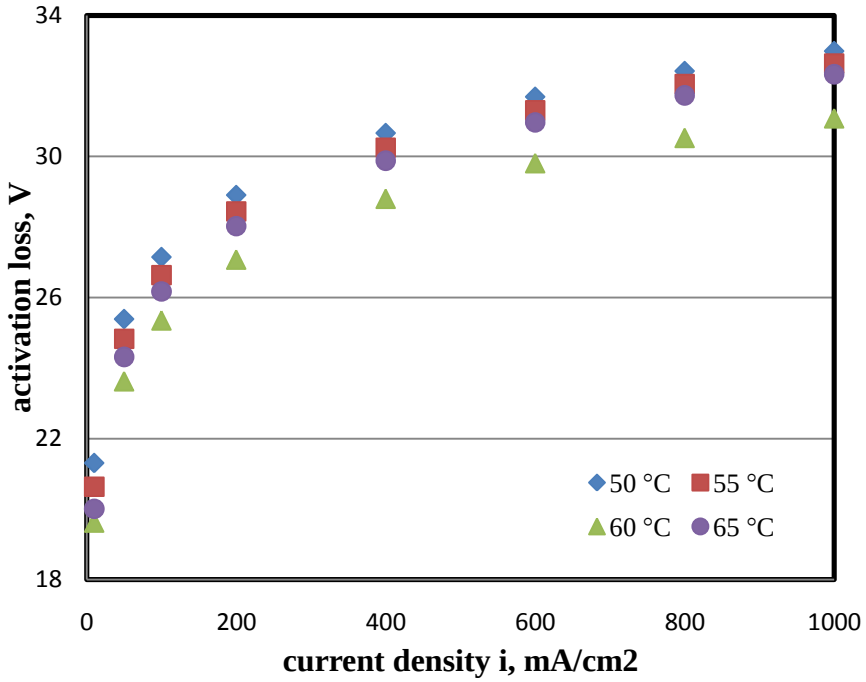

Figure 5.21. Activation loss variations with different temperatures

Another undesirable effect also arised at the ohmic loss term. The ohmic loss at 60 °C was found higher than at 55 °C. The ionic resistance linearly increases with the load from 10 to 1000 mA/cm^2 (Figure 5.22).

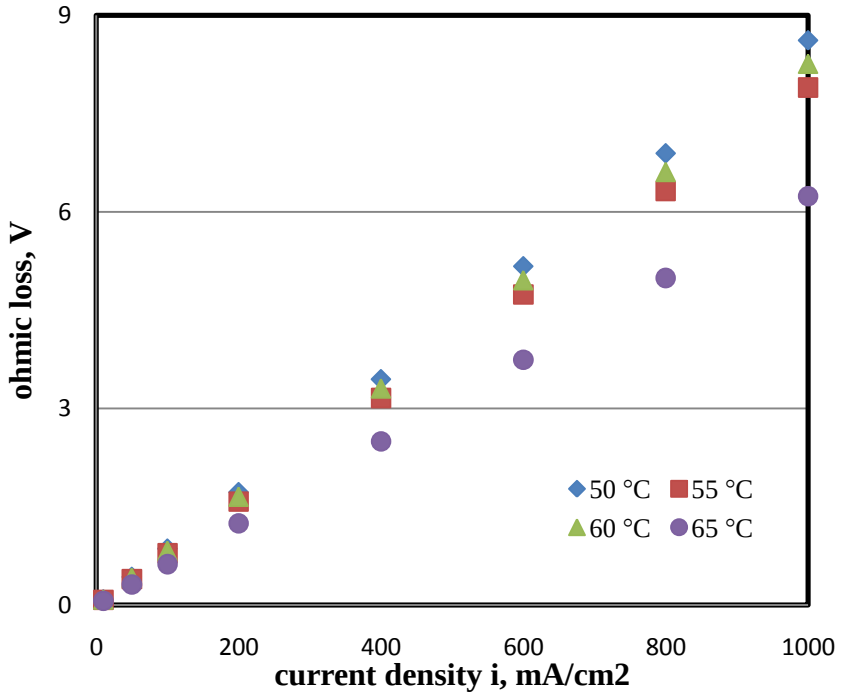

Figure 5.22. Ohmic loss variation with different temperatures

Due to the relative humidity variation values are close to each other from 75% to 95% for constant temperature and stoichiometry, the effects could not be clearly observed. The relativity humidity has effects on ohmic loss than activation loss providing the humid membrane media for proton pass. However the observations found results which has a slightly higher ohmic loss at higher relative humidity (95% RH) than the others that in reality the proton transfer inside membrane should improve with high humidity range.

To better understand the model polarization losses variation with different operation regimes, the parameters inside the model should be investigated. The following graphs show only the parameters i_o, α and R_{int} which are dependent on temperature (Figure 5.23, 5.24, 5.25 respectively). The relative humidity effects on model parameters are not presented due to the lack of reasonable results. Before the graphs, the estimated parameters from the model and coefficient of determination results are presented at Table 5.7.

Table 5.7. Model parameters and coefficient of determination (R^2) results according to different test conditions

Test Conditions	**α**	**i_o (mA/cm^2)**	**R_{int} (ohmcm^2)**	**R^2**
50°C /RH 95%	0,4173	0,00224	0,1149	0.99937
55°C /RH 95%	0,4118	0,00365	0,1053	0.99910
60°C /RH 95%	0,4379	0,00378	0,1101	0.99943
65°C /RH 95%	0,412	0,00564	0,0831	0.99891
60°C /RH 85%	0,4223	0,00513	0,0966	0.99934
60°C /RH 75%	0,4378	0,00297	0,0949	0.99960

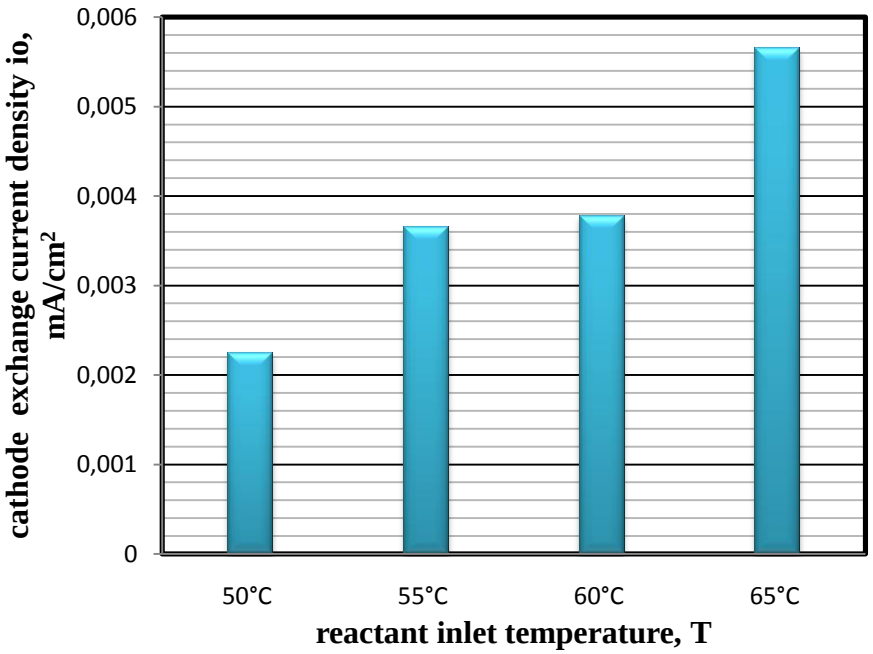

Figure 5.23. Cathode exchange current density versus reactant inlet temperature

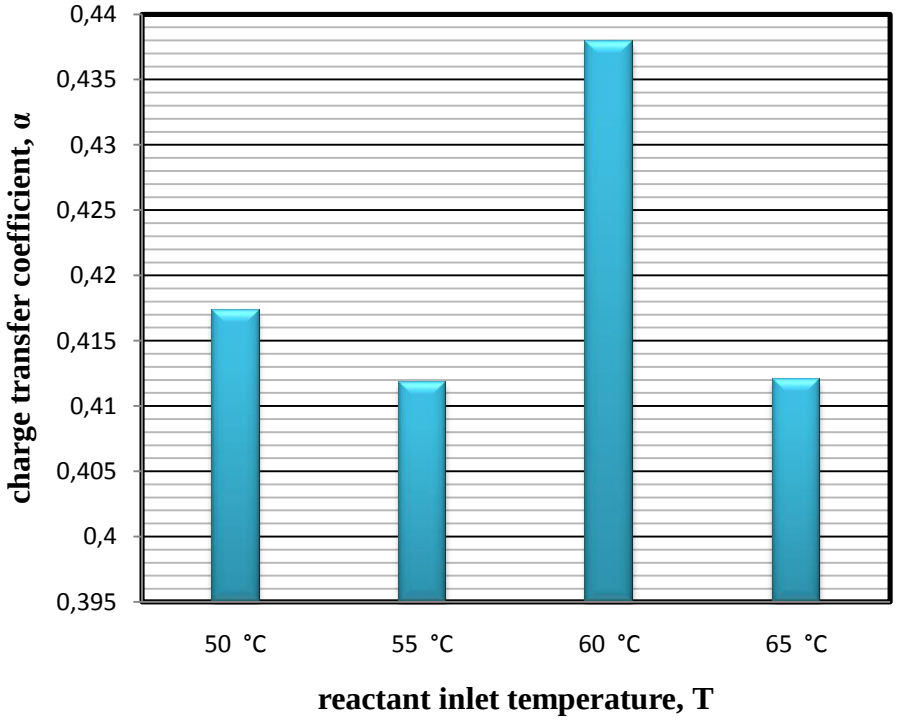

Figure 5.24. Charge transfer coefficient versus reactant inlet temperature

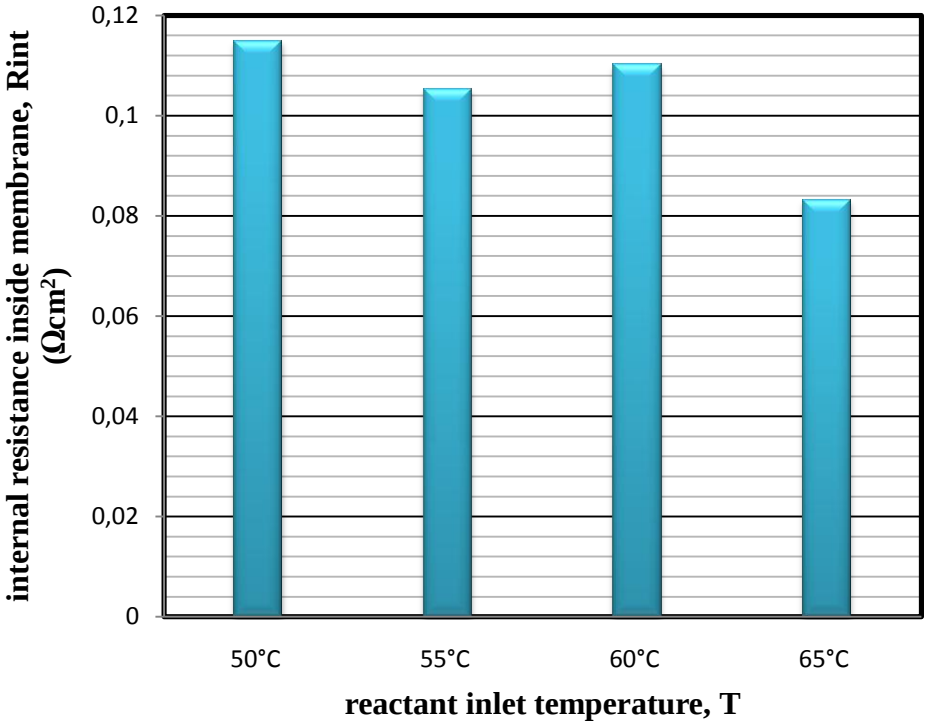

Figure 5.25. Membrane internal resistance versus reactant inlet temperature

Figure 5.23 shows that the cathode side exchange current density was found between 0.002 and 0.006 mA/cm^2 . In literature, the cathode exchange current density value varies in a wide range. Springer et al. (1991) found a high value, 10 mA/cm^2 , it could be due to the fact that the cathode is fed with pure oxygen instead of air. On the other hand it was found really low value as 4.84×10^{-5} mA/cm^2 that could be explained with the materials of the electrodes different from the usual carbon cloth (You and Liu, 2001 and 2002). As indicated from the values given in Figure 5.23, the exchange current density increases as the reaction temperature increases. Similar behaviour is shown by Santarelli et al.(2006) and Parthasarathy et al.(1992) research increasing from $i_{o,c} = 6\times10^{-2}$ mA/cm^2 at T=30 °C to $i_{o,c} = 2.6 \times 10^{-1}$ mA/cm^2 at T=70 °C. The increase in temperature enhances the rate of reaction including the forward and reverse rates at equilibrium and hence i_o increases (Haji, 2011). Bevers et al. (1997) found the exchange current density value 1×10^{-6} A/cm^2 that is close to the observed values in this study (Santarelli et al., 2006). Figure 5.24 shows the cathode transfer coefficient values that were found close to each other for different temperatures from 50 to 65 °C. This parameter typically has the value around 0.4 for cathode that represents the proportion of energy available at the electrode that is used in the electrochemical reaction (Costa et

al., 2006). Larminie and Dicks (2003) consider the value of $\alpha_{cathode}$ to range from 0.2 to 0.5 in most circumstances. A well-designed fuel cell would have R_{int} in the range of 0.05-0.1 Ω cm^2 while values between 0.1 and 0.2 Ω cm^2 are considered typical. In this study the values for internal resistance are consistent as in the range of the typical values. However in literature, resistance values were observed much higher from 0.2 up to 0.6 Ωcm^2 depending on the types of membrane, temperature and membrane humidification. Thinner Nafion membrane decreases ohmic resistance therefore it was observed that the Nafion 117 has a higher internal resistance than Nafion 115 and Nafion 112 (Tazi and Savadogo, 2000). As mentioned previously, at the properties of test object for polarization tests, the manufacturer does not reveal the properties of the stack inside components. Therefore, at my study, the lower resistance could be attributed to the use of low thickness membranes like Nafion 112 or 115. The membrane specific resistivity r_M that defines ohmic resistance with thickness (Equation 2.18) is a function of many variables such as temperature and degree of humidification of the membrane. It should decrease with the membrane humidification. The resistance R_{int} decreases with temperature. Kim et al. (1995) considering a Nafion 115 membrane at different temperatures and pressures in case of p=1 atm at T= 50 °C, the resistance is evaluated as R_{int} = 0.363 Ω cm^2 and T= 70 °C as R_{int} = 0.238 Ω cm^2 . In this study, except the operation condition for 60 °C the ohmic loss decrease exists with increasing temperature (Figure 5.25). For the case 60 °C, the reason of deviation is not explained clearly and it requires to be repeated the same test to understand whether the problem is about the operation state at that day or not.

CHAPTER 6

CONCLUSION

In this study, 10 kW peak power proton exchange membrane fuel cell (PEMFC) stack characteristic (i-V polarization) curve was investigated by varying operation conditions. Then experimental data are fitted into an early developed analytical model where the output stack voltage is a function of thermodynamic reversible voltage and activation, ohmic and concentration losses describing the polarization curve characteristics.

The test module was constituted for the experimental validation of polarization curve testing procedures within the framework of the EU-funded Project FCTESNET. PEM stack composed of 75 single cells with 200 cm^2 active catalyst area manufactured by NedStack. A pure hydrogen for anode electrode and an air for cathode electrode as reactants fed into the stack. The test procedure is composed of a few steps in turn; start-up, conditioning and lastly test output measurement. It is essential to provide the stabilization of test inputs and outputs during conditioning step before test output measurement. The tests were started descending from (step down) 1000 mA/cm^2 to 10 mA/cm^2 with 8 current density steps and followed arising (step up) to the same current density (1000 mA/cm^2) proceeding the same path. At each current density step, the average output stack voltage was recorded. For the test results, only the step down data were evaluated. The tests were operated at a range of temperatures from 50°C to 65°C with constant pressure, stoichiometry and reactant inlet relative humidities for one data series in order to analyse the temperature effects on polarization curve and another data series were applied with different inlet relative humidities simultaneously both for cathode and anode electrodes from 75% to 95%, holding constant the other operation conditions.

In the model, the thermodynamic voltage was calculated based on the Nernst Equation and its average value taken from the step down current density corresponding values was used for data fitting into semi-empirical nonlinear model. For data fitting, LABFIT curve fitting (nonlinear regression program) software was used with Levenberg Marquardt algorithm. In this study, the model merely includes the activation

and ohmic losses. The concentration losses term in the model was neglected due to the fact that tests were not able to reach this logaritmic loss area presented mostly at high current density values and the anodic activation loss was also neglected because anode electrode has rather order of magnitude higher kinetics than cathode electrode. The model parameters that function the minimisation of the difference between experimental and model stack voltage values were identified by fitting. These are charge transfer coefficient and ionic exchange current density for activation loss and internal resistance for ohmic loss. The concepts and variations of these parameters by temperature were examined and compared with published literature values to obtain the meaningful results. The relative humidity effect on model parameters could not give any reasonable results that could be assumed by the limited number of relative humidity values and their closeness to each others.

The cathode exchange current density values increase with reactant inlet temperature coherently with literature definition and the values were also found in the range of literature increasing from 2.247×10^{-6} A/cm^2 at T=50 °C to 5.643×10^{-6} A/cm^2 at T=65 °C. The charge transfer coefficient value was also found in the range of literature around 0.4. The internal resistance gradually decreases when the temperature increases and the lower internal resistance value found around 0.1 Ωcm^2 proves the lower ohmic loss. The model coefficient of determination results were also pointed out .

In the conclusion of this study it is obtained that a nonlinear semi-empirical model can reasonably model the i-V polarization curve of a PEM fuel cell stack. The experimental data fitting into model is proven by reasonable model parameter values and the coefficient of determination results. The temperature effect onto voltage loss as activation loss and ohmic loss also demonstrated although temperatures are close to each other.

REFERENCES

Al-Baghdadi, M.A.R.S. (2005). Modelling of proton exchange membrane fuel cell performance based on semi-empirical equations', *Renewable Energy, 30,* 1587-1599.

Amirinejad, M., Rowshanzamir, S., Eikani, M.H. (2006). Effects of operating parameters on performance of a proton exchange membrane fuel cell. *Journal of Power Sources, 161,* 872-875.

Amphlett, J.C., Baumert, R.M., Mann, R. F., Peppley, B. A. and Roberge, P. R. (1995). Performance modeling of the Ballard Mark IV solid polymer electrolyte fuel cell. I. Mechanistic Model Development. *Journal of The Electrochemical Society, 142,* 1-8.

Andoura, S. (2007). Security of supply and the external dimension of a European energy policy?. *Studia Diplomatica: LX, no:2, EGMONT-Royal Institute for International Relations*, Brussels.

Barbir, F. (2005). *PEM fuel cells:Theory and Practice*. Acamic Press.

Barbir, F. (2008). Fuel cell basic chemistry, electrochemistry and thermodynamics. *Mini-Micro Fuel Cells:Fundamentals and Applications.* Springer .

Basu, S. (2007). *Recent Trends in Fuel Cell science and technology*. India. Anamaya Publishers.

Beden, A. (2007). Security of energy supply in the EU: Challenges and solutions. İstanbul. Institut Europeen Des Hautes Etudes Europeennes et Internationales.

Bernardi, D.M. and Verbrugge, M.W. (1992). A mathematical model of the solid polymer electrolyte fuel cell. *Journal of The Electrochemical Society 139 (9),* 2477- 2491.

Berning, T. and Djilali, N. (2003). Three-dimensional computational analysis of transport phenomena in a PEM fuel cell-a parametric study. *Journal of Power Sources 124,* 440-452.

Bevers, D., Wohr, M., Yasuda, K., Oguro, K. (1997). Simulation of a polymer electrolyte fuel cell electrode. *Journal of Applied Electrochemistry 27,* 1254-1264.

Bleischwitz, R., Fuhrmann, K. (2006). Introduction to the special issue on hydrogen in energy policy. *Energy Policy 34* , 1223-1226.

Cook, B. (2001). An introduction to fuel cells and hydrogen technology. Canada. Heliocentris.

Costa, R.A., Camacho, J.R., Guimaraes, Jr.S.C. and Salerno C.H. (2006). The polymer electrolyte membrane fuel cell as electric energy source, steady state and dynamic behaviour. Brasil.

European Commission Joint Research Centre Institute for Energy Test Results Report, Test No.1b, (2009). Validation of FCTESTNET/FCTES^{QA} TEST Module TM PEFC TM ST5-3: *Testing the voltage and the power as function of the current density (Polarisation curve for a PEFC stack)*. Petten.

European Commission Special Report. (2003). Hydrogen energy and fuel cells: A vision of our future. Brussels.

Fowler, M.W., Mann, R. F., Amphlett, J.C., Peppley, B.A., and Roberge, P.R. (2002). Incorporation of voltage degradation into a generalised steady state electrochemical model for a PEM fuel cell. *Journal of Power Sources,106,* 274-283.

Haji, S. (2011). Analytical modeling of PEM fuel cell i-V curve. *Renewable Energy, 36,* 451-458.

Holland B.J., Zhu J.G., Jamet L. (2007). Fuel cell technology and application. University of Technology. Sydney.

International Energy Agency (IEA) Report (2004). Hydrogen & Fuel Cells review of National R&D Programs. France. OECD/IEA.

International Energy Agency (IEA) Report (2007). Energy security and climate policy. France. OECD/IEA.

International Partnership for the Hydrogen Economy. Hydrogen Production and Delivery Fact Sheet. *www.iphe.net*

Kazım, A. (2004). Determination of an optimum performance of a PEM fuel cell based on its limiting current density. *Hydrogen Materials Science and Chemistry of Carbon Nanomaterial,* Kluwer Academic Publishers.

Kim, J., Lee, S.M., Srinivasan, S. and Chamberlin, C.E. (1995). Modelling of proton exchange membrane fuel cell performance with an empirical equation. *Journal of The Electrochemical Society, 142*, 2670-2674.

Kuang, K., Easler, K. (2007). *Fuel Cell Electronics Packaging*, Introduction to fuel cell technology. Springer .

Larminie, J. and Dicks, A. (2003). *Fuel Cell Systems Explained (2nd edition)*, John Wiley&Sons.

Leon, A. (2008). *Hydrogen Technology Mobile and Portable Applications*. Springer.

Mann, R.F., Amphlett, J.C., Hooper, M.A.I., Jensen, H.M., Peppley, B.A., Roberge P. R. (2000). Development and application of a generalised steady state electrochemical model for a PEM fuel cell. *Journal of Power Sources, 86*, 173-180.

Mench, M. (2008). *Fuel Cell Engines*. John Wiley &Sons.

Mo, Z.J., Zhu, X.J., Wei, L.Y. and Cao G.Y. (2006). Parameter optimization for a PEMFC model with a hybrid genetic algorithm. *International Journal of Energy Research, 30*, 585-597.

Moreira, Marcos V., Da Silva, Gisele, E. (2009). A practical model for evaluating the performance of proton exchange membrane fuel cells. *Renewable Energy, 34*, 1734-1741.

Nguyen, T.V. and White, R.E. (1993). A water and heat management model for proton exchange membrane fuel cells. *Journal of The Electrochemical Society, 140(8)*, 2178-2186.

Parthasarathy, A., Supramaniam, S., Appleby, A. J., Martin, C. R. (1992). Temperature dependence of the electrode kinetics reduction at the Platinum/Nafion interface-a microelectrode investigation. *Journal of The Electrochemical Society, 139*, 2530-2537.

Pasricha, S., Keppler, M., Shaw, S. R. and Nehrir, M. H. (2007). Comparison and identification of static electrical terminal fuel cell models. *IEEE Transactions on Energy Conversion, 22 (3).*

Rayment, C., Sherwin, S. (2003). Introduction to Fuel Cell Technology. University of Notre Dame. USA.

Riis, T., Hagen, E.F., Vie, P.J.S., Ulleberg Ø. (2005). Hydrogen Production -Gaps and Priorities. IEA Hydrogen Implementing Agreement (HIA). Norway.

Rowe, A. and Li, X. (2001). Mathematical modeling of proton exchange membrane fuel cells. *Journal of Power Sources, 102,* 82-96.

Santarelli, M.G., Torchio, M.F., Cochis, P. (2006). Parameters estimation of a PEM fuel cell polarization curve and analysis of their behavior with temperature. *Journal of Power Sources, 159,* 824-835.

Springer, T.E., Zawodzinski, T.A. and Gottesfeld, S. (1991). Polymer electrolyte fuel cell model. *Journal of the Electrochemical Society, 138(8),* 2334-2341.

Tazi, B., Savadogo, O. (2000). Parameters of PEM fuel cells based on new membranes fabricated from Nafion®, silicotungstic acid and thiophene. *Electrochimica Acta, 45,* 4329-4339.

U.S. Department of Energy Hydrogen Program (2006).Hydrogen Storage.U.S.A.

Wishart, J., Dong, Z. and Secanell, M. (2006). Optimization of a PEM fuel cell system based on empirical data and a generalized electrochemical semi-empirical model. *Journal of Power Sources,161,*1041-1055.

Xia, Z.T., Chan, S.H. (2007). Analysis of carbon-filled gas diffusion layer for H_2/air polymer electrolyte fuel cells with an improved empirical voltage-current model. *International Journal of Hydrogen Energy, 32,* 878-885.

Yan, Q., Toghiani, H., Causey, H (2006). Steady state and dynamic performance of proton exchange membrane fuel cells (PEMFCs) under various operating conditions and load changes. *Journal of Power Sources, 161,* 492-502.

Yi, J.S., Van, Nguyen, T. (1999). Multicomponent transport in porous electrodes of proton exchange membrane fuel cells using the interdigitated gas distributors. *Journal of The Electrochemical Society, 146(1),* 38-45.

You, L. and Liu, H. (2001). A parametric study of the cathode catalyst layer of PEM fuel cells using a pseudo-homogeneous model. *International Journal of Hydrogen Energy, 26,* 991-999.

You, L. and Liu, H. (2002). A two-phase flow and transport model for the cathode of PEM fuel cells. *International Journal of Heat Mass Transfer, 45,* 2277-2287.

Yuan, X. Zi., Song, C., Wang, H., Zhang, J. (2009). *Electrochemical Impedance Spectroscopy in PEM Fuel Cells:Fundamentals and Applications*. Springer.

APPENDIX A

COMPONENTS OF THE TEST SETUP INCLUDING TYPES OF SENSORS AND LOCATION

Description	Type	Sensor/Calc
Stack Temperature	Thermocouple type K	T-5
Coolant mass flow rate	MFC Burkert 8035	F-3
Gas pressure at outlet port	Pressure transducer Druck	Fuel:P-5 Oxidant:P-6
Gas temperature at fuel inlet	Thermocouple type K	T-2
Gas temperature at oxidant inlet	Thermocouple type K	T-3
Stack current	TDI Dynaload bank	I-0
Fuel flow	MFC Brooks 5853s	F-1
Oxidant flow	MFC Brooks 5853s	F-2
Stack voltage	TDI Dynaload bank	U-0
Individual cell voltages	FCATS HFR* system	U-1…U-90
Gas temperature at fuel outlet	Thermocouple type K	T-6
Gas temperature at oxidant outlet	Thermocouple type K	T-7
Stack coolant inlet temperature	Thermocouple type K	T-4
Stack coolant outlet temperature	Thermocouple type K	T-5
Coolant inlet –outlet temperature difference	Calculated	T-5-T-4
Pressure drop in fuel flow path	DPT (differential pressure transducer) PMP4170	P-5-P-1
Pressure drop in oxidant flow path	DPT Druck PMP4170	P-6-P-2
Pressure drop in coolant flow path	DPT Druck Type PMP4170	P-4-P-3

*High Frequency Resistance

APPENDIX B

TIME CONSTANTS AND VARIABLES RELATED TO DATA ACQUISITION

Symbol	Description	Value	Unit
t_k	Start time of interval k, belonging to set point k	-	(s)
t_{int}	Interval between set points	15	(min)
t_{eq}	Equilibration time before start of data acquisition	10	(min)
t_{offs}	Interval between the end of the data acquisition time period for interval k ($t_{k,m-1}$) and beginning of the next interval k+1	0.5	(min)
t_{acq}	Time period for data acquisition	$t_{int} - t_{eq}$- t_{offs}	(min)
t_{smpl}	Data acquisition sampling interval	10	(s)
m	Number of data points per interval k	$\frac{t_{acq}}{t_{smpl}}$ +1	-
$t_{k,l}$	Data acquisition time points	$t_k +$ $t_{eq}+lt_{smpl}$	(s)